

DATE 1990-11-15 DEAN

The Electronic Response of 2,2,4,4 Tetramethylpentane  
to Minimum Ionizing Particles

by

Yuhang Li

B.Sc., University of Science and Technology of China, 1983  
M.Sc., Institute of High Energy Physics, Academia Sinica, 1986

A Thesis Submitted in Partial Fulfillment of the  
Requirements for the Degree of  
MASTER OF SCIENCE  
in the Department of Physics and Astronomy

We accept this thesis as conforming to the required standard

Dr. Richard K. Keeler, Supervisor

Dr. Lyle P. Robertson, Supervisor

Dr. Alan Astbury, Department Member

Dr. Alexander D. Kirk, Outside Member

Dr. David A. Harrington, External Examiner

©Yuhang Li, 1990

University of Victoria

*All rights reserved. Thesis may not be reproduced in whole or in part,  
by mimeograph or other means, without the permission of the author.*

QC702

L5

Supervisors: Dr. Richard Keeler and Dr. Lyle Robertson

ABSTRACT

Liquid hydrocarbons have been suggested as a detection media for ionization chambers in hadronic calorimeters as a means of improving their energy resolution.

In this thesis, the performance of a parallel plate (with 1 cm separation) ionization chamber using room temperature 2,2,4,4 TMP was studied using minimum ionizing cosmic rays.

We obtained the drift mobility of the ionization electrons  $\mu = 26.3 \pm 0.8 \text{ cm}^2\text{V}^{-1}\text{s}^{-1}$ , the lifetime of the electrons  $\tau_l = 121 \pm 19 \text{ }\mu\text{s}$ , and the free ion yield as a function of electrical field with  $G_{fi}(0) = 0.743 \pm 0.029 \text{ electrons}/100 \text{ eV}$  at 293 °K, by a waveform analyzing method.

Examiners:

[Redacted]

Dr. Richard Keeler, Supervisor

[Redacted]

Dr. Lyle Robertson, Supervisor

[Redacted]

Dr. Alan Astbury, Department Member

[Redacted]

Dr. Alexander Kirk, Outside Member

[Redacted]

Dr. David Harrington, External Examiner

# Contents

Table of Contents . . . . .	iii
List of Figures . . . . .	v
List of Tables . . . . .	vii
Acknowledgements . . . . .	viii
<b>1 Introduction</b>	<b>1</b>
<b>2 Principle of a Liquid Ionization Chamber</b>	<b>6</b>
2.1 Working Principle . . . . .	6
2.2 Ionization Energy Loss in a Medium . . . . .	7
2.3 Ion Yield and Recombination . . . . .	10
2.3.1 Ion Yield . . . . .	10
2.3.2 Onsager Theory . . . . .	11
2.3.3 Theoretical Formula for Free Ion Yield . . . . .	12
2.4 Attachment . . . . .	14
2.5 Ion Drift in Liquid . . . . .	15
2.6 The Signal of the Electron Component . . . . .	16
<b>3 TMP Purification</b>	<b>18</b>
3.1 The TMP Test Cell and Purification System . . . . .	18
3.2 Test Cell Preparation . . . . .	21
3.3 Filter Preparation . . . . .	22
3.4 Purification Process . . . . .	23

<b>4</b>	<b>Cosmic Ray Telescope and Electronics</b>	<b>24</b>
4.1	Faraday Cage . . . . .	24
4.2	Telescope . . . . .	25
4.2.1	Plateau and Timing of Counters . . . . .	25
4.2.2	Event Selection by the Telescope . . . . .	28
4.2.3	Estimation of Event Rate . . . . .	29
4.2.4	Mean Path of Triggering Muon in TMP . . . . .	32
4.3	The Electronics System . . . . .	32
4.3.1	Arrangement of Electronics . . . . .	32
4.3.2	Data Acquisition System . . . . .	34
4.3.3	Impulse Response of the System . . . . .	35
4.3.4	Charge Sensitivity . . . . .	43
<b>5</b>	<b>The Mobility and Lifetime of Free Electrons</b>	<b>48</b>
5.1	Theoretical Formula of Waveform . . . . .	48
5.2	Noise, Data Acquisition, and Initial Cuts . . . . .	49
5.3	Fits . . . . .	52
5.4	Systematic Errors . . . . .	54
<b>6</b>	<b>Effect of Field on Free Ion Yield</b>	<b>61</b>
6.1	Method to Measure $G_{fi}(E)$ . . . . .	61
6.2	Calculation of the Most Probable Energy Loss of Cosmic Ray Muons in the Test Cell . . . . .	62
6.3	The Most Probable Number of Electrons . . . . .	63
6.4	$G_{fi}(E)$ Curve and Fitted $G_{fi}(0)$ . . . . .	68
<b>7</b>	<b>Conclusion</b>	<b>71</b>
	Bibliography . . . . .	73

# List of Figures

2.1	Energy loss rate of muon in TMP . . . . .	9
3.1	The test TMP cell . . . . .	19
3.2	The Vacuum system . . . . .	20
3.3	M. S. Filter . . . . .	22
4.1	Faraday cage . . . . .	25
4.2	Cosmic ray telescope . . . . .	26
4.3	Plateau of counters . . . . .	27
4.4	Solid Angle . . . . .	30
4.5	Muon momentum density distribution at sea level . . . . .	31
4.6	Distribution of path in TMP . . . . .	33
4.7	Arrangement of electronics . . . . .	34
4.8	Idealized electronic chain . . . . .	36
4.9	R(t): data and fitted curve (slow sweep) . . . . .	42
4.10	R(t): data and fitted curve (fast sweep) . . . . .	43
4.11	Measured charge sensitivities . . . . .	46
4.12	Capacitance as a function of amplitude . . . . .	47
5.1	A sample of measured pulses . . . . .	50
5.2	Variance with cut for 3.5 kV data . . . . .	51
5.3	1/td as a function of field . . . . .	54
5.4	Average wave form and fitted curve at 250 V . . . . .	55

LIST OF FIGURES

5.5	$v(t)$ vs $t/td$ for various $\tau_l$ at 1000 V . . . . .	57
5.6	$v(t)$ vs $t/td$ for various $\tau_l$ at 250 V . . . . .	58
5.7	$\mu$ vs $\tau_l$ for various HV . . . . .	59
6.1	$Slope_{pre}$ vs. $Slope_{post}$ . . . . .	64
6.2	$Level_{pre}$ vs. $Level_{post}$ . . . . .	65
6.3	Pulse height histogram and fitted curve at 250V . . . . .	66
6.4	Pulse height data and Monte Carlo at 1500 V . . . . .	68
6.5	Free ion yield: data and fitted curve . . . . .	70

# List of Tables

1.1	Structural formula of 2,2,4,4 TMP . . . . .	3
1.2	Properties of 2,2,4,4 TMP (at 293 K except indicated) . . . . .	4
4.1	Results of impulse function fit . . . . .	41
4.2	Fitted results of input and output pulses . . . . .	44
4.3	The charge sensitivities . . . . .	45
5.1	Number of pulses used at each high voltage . . . . .	52
5.2	Results of global fitting . . . . .	56
5.3	Summary of systematic error analysis. Parameter values in parentheses indicate that those parameters were held fixed in the fit. . . . .	60
6.1	The most probable charge at different field . . . . .	69
7.1	Comparison of $\mu$ and $G_{f_i}(0)$ measurements in room temperature 2,2,4,4 TMP . . . . .	72
7.2	Comparison of $\mu$ and $G_{f_i}(0)$ of 2,2,4,4 TMP with other candidates . . . . .	72

## ACKNOWLEDGEMENTS

I am greatly indebted to my supervisors, Dr. Richard Keeler and Dr. Lyle Robertson, and supervisory committee member, Dr. Alan Astbury, for encouraging me in my studies and for suggesting to me that I join this research work.

Dr. Richard Keeler's and Dr. Paul Poffenberger's generous support and valuable guidance in various stages of my work have been very much appreciated.

My thanks are also due to Paul Schenk and Lynda Wong for their help with the computer, and to all of the other people involved in this project.

# Chapter 1

## Introduction

The use of room temperature liquids as detection media in ionization chambers dates back to late last century when J. Thomson observed the increase in the electrical conductivity of vaseline oil under the action of X-rays [1]. However, the operation of liquid ionization chambers was based on the measurement of ionic current at that time. It is less convenient to use that type of room temperature liquid chambers in high energy physics.

In the late 1960's, the high mobility of electrons in ultrapure hydrocarbons was discovered [2] [3] [4]. It opened up the possibility of operating ionization chambers at room temperature in pulse mode, i.e. detecting the electronic component of the ionization produced by the passage of an ionizing particle or photon. Since then, the development and applications of liquid ionization chambers in high energy physics have grown rapidly because of the many advantages from liquids. These advantages include high density, which yields good energy absorption and very high spatial resolution compared with gas, the availability of very large continuous volumes at low cost, the uniformity and the reproducibility of charge collection, and the prospect of reaching energy resolutions approaching semiconductor detector performance.

In recent years, the particular motivation of studying room temper-

ature hydrocarbon liquids as possible ionization media is the rapid development of hadronic calorimetry technology, because large hadronic calorimeters will be key instruments for particle detection in the next generation of experiments at colliding-beam accelerators.

The response of a hadronic calorimeter to an incident hadron is smaller than that to a lepton with same energy [5] [6]. This fact is expressed by

$$h/e < 1 \quad (1.1)$$

where  $h$  denotes the response to a hadron, which could be for instance a pion ( $\pi$ ) or a proton ( $p$ ), and  $e$  denotes the response to an electron of the same energy.

Let's consider the case of the  $\pi/e$  ratio. After a high energy electron enters a calorimeter, the dominate process of energy loss is the electromagnetic cascade (EMC), bremsstrahlung for electrons and positrons, and pair production for photons. Until the energy of the secondary particles drops down below a small threshold energy, all of the deposited energy is detectable. For an incident charged pion, the dominate process of energy loss is the hadronic cascade (HC), multi-particle generation by inelastic nuclear interactions. The secondary particles include charged hadrons, nuclear fragments, muons, neutrinos, and an electromagnetic cascade component which is contributed to by decay of secondary  $\pi^0$ 's to pairs of gammas ( $\gamma$ ). The loss of signal from low energy neutrons, neutrinos and binding energy in HC is the reason why the calorimeter signal of a pion is less than that of an electron. The measured ratio of  $\pi/e$  was about 0.6-0.7 in a sampling calorimeter with Fe, Cu and Pb at 10 GeV [6]. The missing energy and its fluctuation causes worse energy resolution for hadron energy measurement in hadronic calorimeters.

If  $h/e$  was increased, the resolution of the hadron calorimeter would



short signal collection time. Among the room temperature liquid hydrocarbons, 2,2,4,4 tetramethylpentane (TMP) is one under consideration. TMP possesses abundant hydrogen and possesses other properties which make it a suitable candidate as an ionization media (see table 1.2). Now several groups in the world have been involved in studies of properties of ionization chambers using 2,2,4,4 TMP as well as other liquid hydrocarbons [9] [10] [11] [12].

Another obvious benefit of using a room temperature liquid rather than the more commonly used liquid Argon is that a room temperature liquid does not require the use of complex cryogenic systems, which create dead space.

The disadvantages of TMP are that it is flammable and that it must be ultra pure to be usable due to its low electron mobility and ion yield relative to liquid noble gases. A parameter representing the purity of the liquid is the electron lifetime, which represents the mean exponential rate of loss of free electrons to electron scavenging impurities present in the liquid.

The physical properties of 2,2,4,4 TMP are listed in table 1.2.

Properties	Values	References
Density ( $g/cm^3$ )	0.72	[17]
$d\Delta/dx_{MIP}$ (MeV/cm) of muon	1.58	[9]
free ion yield at 0 field	0.71 - 0.83	[8] [14]
$e^-$ mobility ( $cm^2V^{-1}s^{-1}$ )	24 - 29	[8] [14] [16]
dielectric constant $\epsilon$	1.98	[17]
boiling point ( $^{\circ}C$ )	122.7	[17]
melting point ( $^{\circ}C$ )	-66.5	[17]
molecular formula	$C_9H_{20}$	[17]

Table 1.2: Properties of 2,2,4,4 TMP (at 293 K except indicated)

The electron mobility and free ion yield are the most important prop-

erties for TMP as an ionization media. Their values in the table are from previous measurements in radiation chemistry research and they vary over a large range in different measurements. In addition, there are no errors listed with the previous measurements.

In this thesis, we used waveform analysis (WFA, also referred to as transient analysis) of pulses from single minimum ionizing cosmic rays to measure the electron mobility and free ion yield of TMP as well as the achievable electron lifetime. Individual pulses from a test cell exposed to cosmic rays were captured and stored, then analyzed offline to extract the relevant parameters. Chapter 2 introduces the principle of a liquid ionization chamber, energy loss of cosmic rays, and processes affecting the collection of electrons. Chapter 3 describes how we purified the liquid. The experimental apparatus and data acquisition are discussed in chapter 4. The analysis of electron mobility and electron lifetime are discussed in chapter 5, and the calculation of the free ion yield is discussed in chapter 6. The final chapter, 7, is a summary and comparison of our results with results from previous measurements.

## Chapter 2

# Principle of a Liquid Ionization Chamber

### 2.1 Working Principle

The basic structure of a liquid ionization chamber is quite simple. In a typical case, two parallel metal plates (electrodes) are fixed in a container filled with a liquid dielectric. The metal plates are used both for applying high voltage and for collecting signals. The high voltage generates a large electric field between the electrodes. When a charged particle passes through the chamber, it loses energy by colliding with electrons of the atoms of the medium. The primary ionization and excitation leave electron-ion pairs around the track of the incident particle.  $\delta$  rays, ejected electrons with high momentum, also generate secondary ionization. Under the influence of the electric field, the electrons drift to the anode and the positive ions drift to the cathode. The current pulse in the external circuit connected to the electrodes rises immediately and disappears after the charge collection is finished.

The drift time of the electrons is much shorter than that of the positive ions (about  $1/10^5$  for TMP [18]). At the beginning of charge collection, a big pulse is formed, then a long tail follows. The pulse is the electronic

component (electrons drifting) and the tail is the positive ionic component. The electronic component of the signal carries all the relevant information of the incident particle and can be easily analyzed with fast electronics. We are therefore interested only in the collection of electrons, since a high rate of events is common in modern high energy physics experiments.

Assuming that the ionizing particle penetrates the electrodes at  $t = 0$  and at  $t = t_d$  the last electron arrives at the anode, the current induced by electrons as a function of time has a triangular form for uniform drifting electrons:

$$i(t) = i(0)\left(1 - \frac{t}{t_d}\right) = \frac{Q_0}{t_d}\left(1 - \frac{t}{t_d}\right), \quad 0 \leq t \leq t_d, \quad (2.1)$$

where  $Q_0$  is the total charge of the electrons. The drift time  $t_d$  is the time required for an electron to drift across the entire gap.  $t_d$  depends on the external field, the plate gap, and properties of the media.

In addition to the acceleration under the external field toward the electrodes, the motions of the electrons and ions in the liquid also include diffusion, recombination, and attachment, which affect the collection of electrons. In order to accurately collect the information carried by the electronic component, we must understand the above processes clearly.

## 2.2 Ionization Energy Loss in a Medium

The energy loss per unit distance of an ionizing particle passing through a slab of material can be expressed by the Bethe-Bloch formula [19]:

$$\frac{d\Delta}{dx} = \frac{DZ\rho}{A}\left(\frac{z}{\beta}\right)^2 \left[ \ln\left(\frac{2m_e\gamma^2\beta^2c^2}{I}\right) - \beta^2 \right] \quad (\text{MeV/cm}), \quad (2.2)$$

where

$$D = 4\pi N_A r_e^2 m_e c^2 = 0.3070 \quad (\text{MeV cm}^2/\text{g}),$$

$$r_e = \frac{e^2}{4\pi\epsilon_0 m_e c^2},$$

and

$$I \approx 16Z^{0.9} \text{ (eV)}.$$

$I$  is the mean ionization potential of the medium,  $\beta$  is the ratio of incident particle speed to light speed,  $e$  is the charge of an electron,  $ze$  is the charge of the incident particle,  $m_e$  is the mass of an electron,  $N_A$  is Avogadro's number ( $6.022 \times 10^{23}/mol$ ),  $Z$  is the atomic number of the medium atom,  $A$  is the mass number of the medium,  $\gamma = 1/\sqrt{1 - \beta^2}$ , and  $\rho$  is the density of the medium. The ionization energy loss is independent of the mass  $M$  of the incident particle as long as  $M \gg m_e$ . The spin of the incident particle is ignored. The maximum energy transfer in a single collision can be approximated by

$$W_{max} = 2m_e c^2 \beta^2 \gamma^2. \quad (2.3)$$

From the curve of energy loss as a function of kinetic energy (fig 2.1), one sees that the energy loss first decreases very quickly while the energy of the incident particle increases. There is a minimum value for the energy loss at a certain energy, called the minimum ionization energy, and approximately equal to 340 MeV for muons, so a particle carried with such an energy is called a minimum ionization particle (MIP). When the energy increases beyond that point, the energy loss also increases slowly (relativistic rise). Polarization, or density effects (ignored in the Bethe-Bloch formula) causes the curve to enter a plateau for  $\gamma > 10$  in liquid media. The energy loss at the plateau is about 10% more than that of a MIP in liquid [20].

The energy loss calculated by the Bethe-Bloch formula represents a mean energy loss. Because of the statistical property of collision processes, there is a statistical fluctuation around the mean value  $\bar{\Delta}$ . In a thin medium,

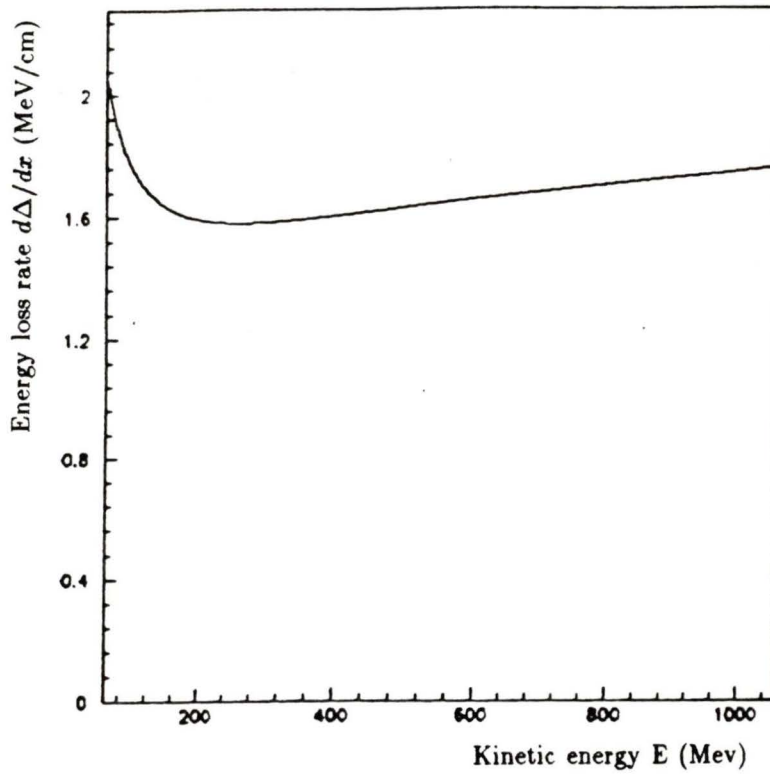


Figure 2.1: Energy loss rate of muon in TMP

the fluctuation of energy loss can be described by either the Landau or Vavilov distribution, depending on  $\kappa$ , which is given by [21]

$$\kappa = \frac{\xi}{W_{max}}, \quad (2.4)$$

where

$$\xi = \frac{2\pi N Z^2 e^4}{m_e v^2} x,$$

and  $x$  is the thickness of the medium.

When  $\kappa < 0.01$ , it is a Landau distribution. When  $0.01 < \kappa < 10$ , it is a Vavilov distribution. For  $\kappa > 10$ , it becomes a Gaussian distribution [22].

## 2.3 Ion Yield and Recombination

### 2.3.1 Ion Yield

There are two types of recombination for electron-ion pairs in liquids. One is initial, or germinate, recombination that is the recombination of an electron with its parent ion (which the electron is from). Another type is columnar recombination that is the recombination of an electron with a positive ion other than its parent ion. Columnar recombination is important for very highly ionizing particles and therefore will not be discussed in this thesis.

In a liquid, after ionization by a charged particle, the positive and negative ions are formed in equal numbers around the track. The number of primary ion pairs produced per 100 eV energy input is defined as the total ion yield  $G_{tot}$ , which is an important physical characteristic quantity of any liquid.

The density of a liquid is much higher than that of a gas, so an electron knocked out from its parent atom collides with its neighboring atoms frequently and slows down quickly. After it becomes thermalized (i.e. its speed drops to the average speed of the molecules), its distance from the parent ion may not be enough to free it from the Coulomb attraction of its parent ion. So, among the initial electron-ion pairs, only a fraction of the electrons escape from the electrical field of their parent ions successfully. The number of such electrons, or separated ion pairs, per 100 eV energy input is defined as the free ion yield  $G_{fi}$ . The free ion yield depends on the total ion yield, as well as the external electric field, temperature of the liquid, and the

rate of energy loss of the incident particle. Obviously, the higher the free ion yield is, the larger the output pulse is.

The relation between the number of escaped electrons  $Q_0$ , the free ion yield  $G_{fi}$  (electrons/100eV), and the total energy loss  $\Delta$  (MeV) is given by

$$Q_0 = 10^4 G_{fi} \Delta. \quad (2.5)$$

### 2.3.2 Onsager Theory

In 1938, Onsager gave a theory [23] for initial recombination to predict the probability of an electron escaping from its parent ion, so initial recombination is also called the Onsager effect. In his theory, once an atom is ionized, the electron loses its outward momentum rapidly by colliding with surrounding molecules due to the high density of a liquid. When the electron becomes thermalized at some distance from its parent ion, it is still affected by the coulumb field of its parent ion. Its movement can then be considered as a Brownian motion under the Coulomb attraction of its parent ion and the external field. The equation of Brownian motion is given by

$$\frac{\partial f}{\partial t} = kT(\mu_1 + \mu_2) \nabla \cdot (e^{-\frac{w}{kT}} \nabla f e^{\frac{w}{kT}}). \quad (2.6)$$

where  $k$  is Boltzmann's constant,  $T$  is the absolute temperature,  $\mu_1$  and  $\mu_2$  are mobilities of the electron and its parent ion respectively,  $w$  is the combined electric potential of the external field and the parent ion, and  $f$  is the concentration of electrons. We can express  $w$  as

$$w = -eEy \cos \theta - \frac{e^2}{\epsilon y} = kT(-2\beta y \cos \theta - \frac{r_c}{y}), \quad (2.7)$$

where

$$r_c = \frac{e^2}{\epsilon kT}, \quad \beta = \frac{eE}{2kT},$$

and where  $E$  is the external field,  $\theta$  is the angle between the direction of the external field and a line connecting the electron and its parent ion,  $\epsilon$  is the dielectric constant of the liquid, and  $y$  is the initial separation distance between the electron-ion pair (the distance at which the electron becomes thermalized). The differential equation and the boundary conditions satisfied by the escape probability  $\varphi$  can be written as:

$$\nabla \cdot (e^{\frac{-w}{kT}} \nabla \varphi(y, \theta)) = 0, \quad (2.8)$$

$$\varphi(0, \theta) = 0, \quad \varphi(\infty, \theta) = 1.$$

Onsager showed that the solution of the above equation is given by:

$$\begin{aligned} \varphi(y, \theta) &= e^{-\beta y(1+\cos\theta)} \int_{s=r_c/y}^{\infty} J_0(2(-\beta y(1+\cos\theta)s)^{1/2}) e^{-s} ds \quad (2.9) \\ &= e^{-r_c/y - \beta y(1+\cos\theta)} \sum_{m,n=0}^{\infty} \beta^{n+m} (1+\cos\theta)^{n+m} \frac{r_c^m y^n}{m!(m+n)!}. \end{aligned}$$

### 2.3.3 Theoretical Formula for Free Ion Yield

Based on Onsager's theory, we can calculate the effect of an external electric field and the temperature on the free ion yield in liquid TMP. First, we expand the term  $e^{-\beta y(1+\cos\theta)}$  in formula (2.9)

$$e^{-\beta y(1+\cos\theta)} = \sum_{l=0}^{\infty} \frac{[-\beta y(1+\cos\theta)]^l}{l!}. \quad (2.10)$$

We rewrite  $\varphi(y, \theta)$  as

$$\varphi(y, \theta) = e^{-r_c/y} \sum_{m,n,l=0}^{\infty} \frac{(-1)^l \beta^{n+m+l} (1+\cos\theta)^{n+m+l} r_c^m y^{n+l}}{l! m! (m+n)!}. \quad (2.11)$$

Since the angle  $\theta$  varies from 0 to  $\pi$ , the average escape probability over all directions is the weighted average:

$$\begin{aligned} \varphi(y) &= \frac{\int_0^\pi \varphi(y, \theta) d\theta}{\int_0^\pi d\theta} \\ &= e^{-\tau_c/y} \sum_{m,n,l=0}^{\infty} \frac{(-1)^l \beta^{n+m+l} r_c^m y^{n+l} \int_0^\pi (1 + \cos\theta)^{n+m+l} d\theta}{l! m! (m+n)! \int_0^\pi d\theta}. \end{aligned} \quad (2.12)$$

If we define  $F(y)$  as the function describing the distribution of initial separation  $y$ , then

$$G_{fi}(E) \propto \int_0^\infty F(y) \varphi(y) dy. \quad (2.13)$$

If the field  $E$  is zero, then

$$\varphi(y) = e^{-\tau_c/y}, \quad (2.14)$$

and

$$G_{fi}(0) \propto \int_0^\infty F(y) e^{-\tau_c/y} dy. \quad (2.15)$$

From

$$\frac{G_{fi}(E)}{G_{fi}(0)} = \frac{\int_0^\infty F(y) \varphi(y) dy}{\int_0^\infty F(y) e^{-\tau_c/y} dy}, \quad (2.16)$$

we obtain

$$G_{fi}(E) = G_{fi}(0) \quad (2.17)$$

$$\sum_{m,n,l=0}^{\infty} \frac{(-1)^l \beta^{n+m+l} r_c^m \int_0^\pi (1 + \cos\theta)^{n+m+l} d\theta \int_0^\infty y^{n+l} F(y) e^{-\tau_c/y} dy}{l! m! (m+n)! \int_0^\pi d\theta \int_0^\infty F(y) e^{-\tau_c/y} dy}.$$

Substituting numerical values and expanding formula (2.17) we have

$$G_{fi}(E) = G_{fi}(0)\left(1 + \frac{9.690E}{\varepsilon T^2} + \frac{35.21E^2}{\varepsilon^2 T^4} - \frac{4.214 \times 10^4 E^2}{\varepsilon T^3} \frac{\int_0^\infty F(y)e^{-r_c/y} dy}{\int_0^\infty F(y)e^{-r_c/y} dy} + \dots\right). \quad (2.18)$$

If we do a plot with a constant temperature, we see that the free ion yield as a function of field is almost linear with a small initial slope  $9.69/\varepsilon T^2$  at low field, and the free ion yield approaches a saturation value which corresponds to the total ion yield as the field goes to infinity.

The distribution  $F(y)$  is unknown, but there exist some good approximations for it. We adopt a Gaussian distribution [7][25][26][27][28]

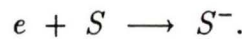
$$F(y) = \frac{4y^2}{\pi^{1/2}b^3} e^{-y^2/b^2}, \quad (2.19)$$

where  $b$  is the most probable value of  $y$ . For room temperature TMP,  $b$  is  $158 \text{ \AA}$  [8].

The definite integrals in formula (2.18) can be calculated by Gaussian Quadrature. Although the integral over  $y$  is from zero to infinity, the integrand approaches zero very fast as  $y$  approaches zero or infinity. We can therefore choose the lower and upper limits of integral range as  $0.1b$  and  $9b$  respectively, and the integral functions are totally covered.

## 2.4 Attachment

The purity of the liquid is very important. Some of the freed electrons encounter electronegative impurities  $S$  while drifting and attach themselves to  $S$  to form negative ions  $S^-$ , which drift much slower than electrons:



Neglecting electron transfer at the electrodes, the rate of decrease of the electron concentration  $n_e$  is given by

$$\frac{dn_e}{dt} = -k_s[S]n_e, \quad (2.20)$$

where  $[S]$  is the concentration of the electron-attaching impurity and  $k_s$  is the bimolecular rate constant. The concentrations are expressed either in  $cm^{-3}$  or in  $mol/l$ . The rate constant  $k_s$  has then either the units  $cm^3/s$  or  $l/(mol\ s)$ . Solving the above equation under the assumption that  $n_e \ll [S]$  leads to the electron concentration as a function of time

$$n_e(t) = n_e(0)e^{-t/\tau_l}, \quad (2.21)$$

where  $\tau_l$  is the lifetime of the electrons given by

$$\tau_l = \frac{1}{k_s[S]}. \quad (2.22)$$

For the electrons, in order to cross the gap of an ionization chamber,

$$\tau_l > t_d$$

has to be met. Electron attachment also influences energy linearity and resolution, so high purity liquid is required.

## 2.5 Ion Drift in Liquid

The remaining electrons, which are accelerated through the liquid by an electric field  $E$ , quickly attain a terminal velocity  $v_d$  which is proportional to the field, if the field is not too large:

$$v_d = \mu E. \quad (2.23)$$

This velocity is also called the drift velocity of an electron.

The electron drift mobility  $\mu$  is given in cm/s per volt/cm, or  $cm^2V^{-1}s^{-1}$ . The value of  $\mu$  is another important characteristic of the medium. The mobility of an electron or single-charged ion is related to the diffusion coefficient  $D$  by the Nernst equation [13]

$$\mu = \frac{De}{kT}, \quad (2.24)$$

where  $e$  is the electron charge,  $k$  is Boltzmann's constant, and  $T$  is the absolute temperature. The mobility is constant at low electric field strengths. For 2,2,4,4 TMP, it is independent of field up to 15 kV/cm at room temperature [14].

## 2.6 The Signal of the Electron Component

From the previous discussion, the output voltage pulse from a chamber as a function of time can be derived. Due to recombination, the initial total charge of the freed electrons corresponding to the free ion yield in liquid becomes field dependent  $Q_0(E)$ . Taking the electron lifetime into account, the total charge of the electrons at time  $t$  in a chamber with field  $E$  is given by

$$Q(E, t) = Q_0(E) \left(1 - \frac{t}{t_d}\right) e^{-t/\tau_e}. \quad (2.25)$$

The induced current is then

$$i(t) = Q(E, t) \frac{v_d}{d} = \frac{Q_0(E)}{t_d} \left(1 - \frac{t}{t_d}\right) e^{-t/\tau_e}. \quad (2.26)$$

The waveform of the voltage pulse output from an idealized charge integrating preamplifier is then expressed by

$$v(t) = \frac{Q_{\text{collected}}(t)}{C_{fb}} = \frac{1}{C_{fb}} \int_0^t i(\theta) d\theta, \quad (2.27)$$

$$= \begin{cases} \frac{Q_0}{C_{fb}} \frac{\tau_1}{t_d} \left[ \left(1 - \frac{\tau_1}{t_d}\right) (1 - e^{-t/\tau_1}) + \frac{t}{t_d} e^{-t/\tau_1} \right] & \text{for } t \leq t_d \\ \frac{Q_0}{C_{fb}} \frac{\tau_1}{t_d} \left[ 1 - \frac{\tau_1}{t_d} (1 - e^{-t_d/\tau_1}) \right] & \text{for } t > t_d \end{cases}$$

where  $C_{fb}$  is the feedback capacitance of the preamplifier.

## Chapter 3

# TMP Purification

### 3.1 The TMP Test Cell and Purification System

A test cell (fig 3.1) was constructed to collect the data for this experiment. The cell is composed of two parallel circular 0.076 cm thick stainless steel plates sealed in a glass chamber connected to a 430 ml glass reservoir. The radius of each plate is 2.54 cm and the distance between the plates is  $1.00 \pm 0.01$  cm. Two stainless steel rods, one from each of the anode and cathode, extend out of the glass wall from the electrodes in opposite directions.

It is known that the concentration of impurities in TMP must be kept extremely low to guarantee a long electron life time, so TMP purification is a key problem in this experiment. In order to get sufficiently pure liquid, the contamination on the surface of the glass walls and steel plates must be removed, as well as the air and vapor in the cell, and most of the impurities, namely water, oxygen, and argon, in the original liquid before filling the TMP into the cell. Therefore, a silica gel and molecular sieve filter and a vacuum system were built to clean the test cell and to purify the TMP before its introduction into the test cell.

The vacuum system, shown in fig 3.2, included two diffusion pump

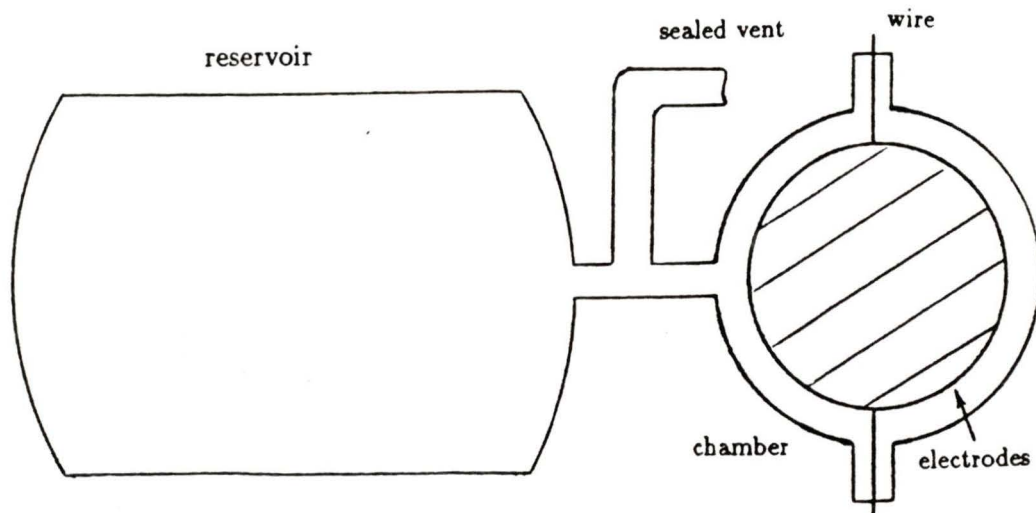


Figure 3.1: The test TMP cell

systems, one used to evacuate the test cell and the other to evacuate the filter. Liquid nitrogen cold traps were used to isolate the TMP-wetted parts of the vacuum system from the pumps in order to avoid contamination of the TMP with pump oil. Aside from several stainless steel bellows valves, the vacuum system was constructed of glass. Glass was chosen for its ease of construction as well as its ease of cleaning. Due to the large gas load of the filter, the bore of the glassware connecting the filter to its pump was made as large as possible to maximize pumping speed. Glassblowing without annealing limited the bore to 2.5 cm diameter. The rest of vacuum system used a smaller bore tube.

The pressure and temperature of the system were monitored by a data acquisition system. Penning gauges, which worked in the high vacuum

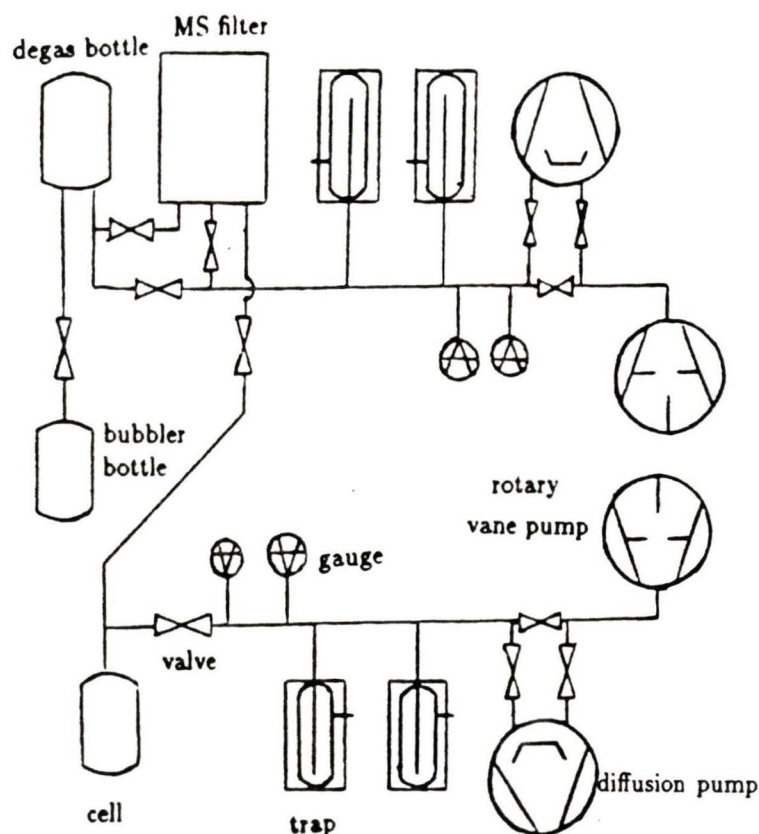


Figure 3.2: The Vacuum system

range, and Pirani gauges, which worked in medium vacuum range, were used for measuring the pressure. Analog voltage signals from the gauge controllers were sent to an analog to digital converter (ADC)<sup>1</sup> in a CAMAC crate for digitization. The digitized voltage was then read and converted into pressure by a program in a PDP-11/34 computer and the pressure-time curve was recorded.

<sup>1</sup>Model 3275, Kinetic Systems

## 3.2 Test Cell Preparation

The first step of the test cell preparation was to electro-polish the electrodes in order to facilitate cleaning. The electro-polishing solution, consisting of 37 % phosphoric acid, 7% water and 56 % glycerin, was subjected to a DC current source of about 3-4 A applied to the electrodes. The polarity was reversed every 5 minutes during the procedure. The test cell was heated by a heat gun during the electro-polishing in order to keep the solution fluid, otherwise, large bubbles would form which would reduce the effectiveness of the procedure. This electro-polishing step took about 90 minutes.

In the next step, the cell was rinsed several times with 95% ethanol, then with distilled water, followed by several rinsings with hot nano-pure water. Argon gas was then passed through the cell to remove the water vapor by evaporation.

Finally, the cell was glassblown onto the vacuum system and pumped to high vacuum. The system was pumped first with the rotary vane pump in the range of rough and medium vacuum (760 to 0.1 torr), and then the diffusion pump was used in the range of high vacuum ( $< 0.1$  torr). The system was not exposed to the rotary vane pump below 0.1 torr in order to minimize backsteaming of rotary pump oil. When the pressure was about  $10^{-4} - 10^{-5}$  torr, the system was baked by thermal tapes uniformly at a temperature up to  $150\text{ }^{\circ}\text{C}$  to remove the gas absorbed on the surfaces. At the final stage, the cell was baked in situ in an oven at  $300\text{ }^{\circ}\text{C}$  while being pumped to remove more gas on the surface of the cell. A base pressure of  $10^{-6}$  torr in the cell was reached after a few days of pumping.

### 3.3 Filter Preparation

In the process of cleaning the TMP, a silica gel and molecular sieve (MS) filter was used to remove most of the electronegative impurities originally contained in the liquid, which was obtained from Wiley Organics<sup>2</sup>. The filter was a mixture of high-purity grade 70-230 mesh silica gel, 4 Å molecular sieve, and 13 X molecular sieve, all contained in a cylindrical glass container of radius 5 cm and height 37 cm. The relative proportions of silica gel : 4 Å MS : 13 X MS were approximately 2 : 1 : 1.

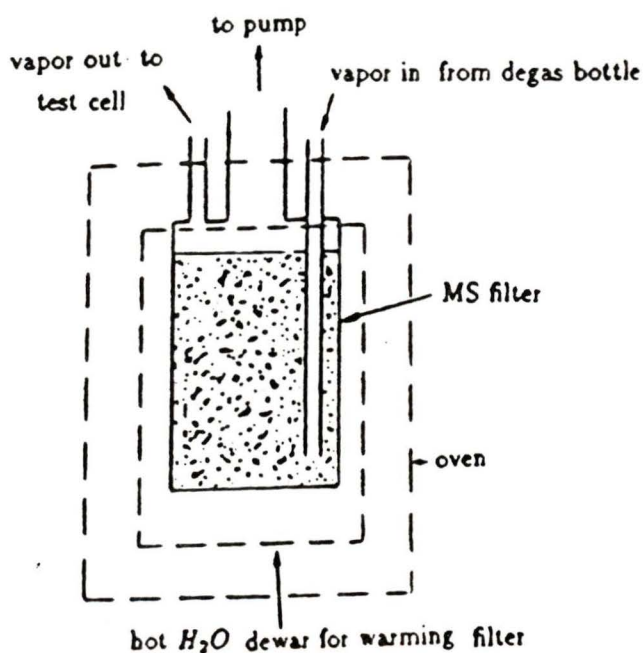


Figure 3.3: M. S. Filter

The filter was prepared by first heating to 300 °C at atmospheric pressure to drive off most of the water vapour absorbed in the silica gel. It

<sup>2</sup>Wiley Organics, Columbus, Ohio, USA

was evacuated to  $1.1 \times 10^{-5}$  torr at  $288^\circ\text{C}$ , over a period of one month. Trapping with  $\text{LN}_2$  started at about  $1.1 \times 10^{-4}$  torr.

After completion of the filter preparation, the rest of the purification system glassware was pumped to about  $10^{-7}$  torr while being heated to about  $150^\circ\text{C}$  with heating tapes.

### 3.4 Purification Process

Once the test cell, filter, and other apparatus were prepared, the procedure to purify the TMP started.

The TMP was first poured through the air into the "bubbler bottle", where it was bubbled vigorously with a flow of argon gas. The argon gas was purified by passage through a getter furnace<sup>3</sup>. This procedure continued for about 30 minutes in order to remove much of the oxygen and nitrogen from the TMP. The bubbler bottle was then sealed and the TMP was transferred into the "degas" bottle by gravity. While in the degas bottle, the TMP was cooled with a liquid  $\text{N}_2$  bath while being pumped, first with the rotary vane pump, and then with the diffusion pump, until the TMP was frozen. The two liquid nitrogen traps isolated the TMP from the pumps at all times. The TMP boiled vigorously during this procedure, thus driving off much of the argon absorbed from the previous step. The TMP was then isolated from the vacuum pumps and allowed to thaw. Once thawed, the "degas" step was repeated one more time. The TMP was finally cryopumped from the degas bottle, through the filter, to the cell by heating the degas bottle and filter and cooling the cell reservoir with a liquid  $\text{N}_2$  bath. About 180 ml of TMP was collected in five hours. The glass neck of the cell was flame sealed and the cell removed from the system.

---

<sup>3</sup>Model 2B-20-Q, Centorr Associates, Inc., Suncook, New Hampshire, USA

## Chapter 4

# Cosmic Ray Telescope and Electronics

### 4.1 Faraday Cage

A cosmic ray telescope was used to trigger on minimum ionizing particles traversing the test cell. The apparatus (see fig 4.1) was shielded in a grounded aluminum Faraday cage. Three scintillator counters were used as the telescope trigger system. Two of the scintillators extended inside the cage, so the reflecting aluminum foil covering their light guides was replaced by white paper to prevent the scintillators acting as antennae for electromagnetic noise. The electrodes of the test cell were oriented horizontally to take advantage of the high rate of events contributed by cosmic rays in the vertical direction.

The design of the test cell proved to be very microphonic, i.e., acoustical noise caused serious signal to noise problems due to fluctuations in the capacitance of the electrodes from vibration of the plates. To damp the vibrations of the cell, an isolation support was constructed. The cage was weighted by some lead bricks and placed on a platform supported by several small innertubes for damping.

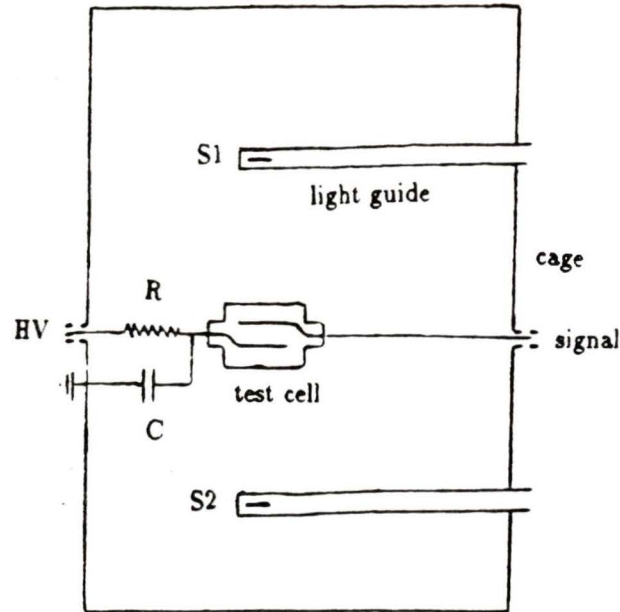


Figure 4.1: Faraday cage

## 4.2 Telescope

A telescope of three plastic NE110 scintillator counters and some absorber material was used to trigger the data acquisition system only on minimum ionizing cosmic rays entering the test cell at near normal incidence. The top two scintillators, S1 and S2, were both of radius 1.55 cm and thickness 0.25 cm. The bottom scintillator, S3, was 10 cm  $\times$  10 cm  $\times$  0.25 cm thick. The telescope is shown schematically in fig 4.2.

### 4.2.1 Plateau and Timing of Counters

The three counters were plateaued using cosmic rays before taking data, i.e., the working voltage of each counter was determined from its efficiency

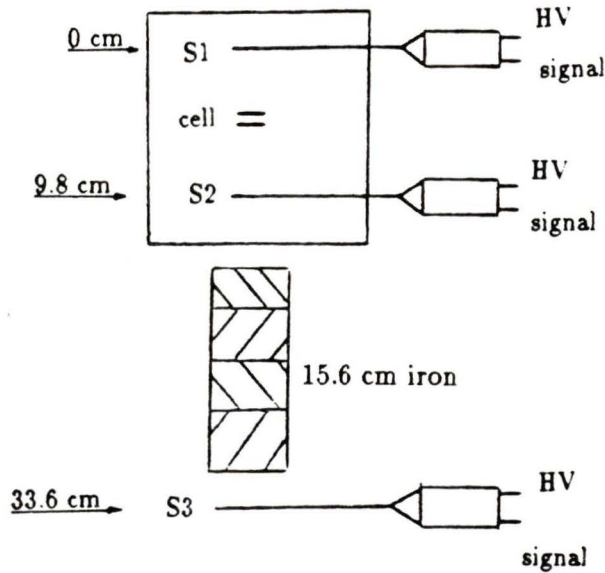


Figure 4.2: Cosmic ray telescope

versus voltage on the photomultiplier, which showed a plateau. In this method, the scintillator  $S$  to be plateaued was placed between two other scintillators  $M1$  and  $M2$ , whose working voltages were already known, and the detection efficiency as a function of high voltage on  $S$  was plotted. The detection efficiency is defined as

$$\epsilon = \frac{N'}{N}, \quad (4.1)$$

where  $N$  is the number of coincidence counts for  $M1$  and  $M2$  only, and  $N'$  is the number of coincidence counts for all of three counters. The statistical error on the efficiency is given by

$$\sigma = \sqrt{N\epsilon(1 - \epsilon)} = \sqrt{\frac{N'(N - N')}{N}}. \quad (4.2)$$

The working voltage for each counter was chosen as 300 V higher than the value at half height of the  $\epsilon$ -HV plateau. One of the measured plateaus is shown in fig 4.3.

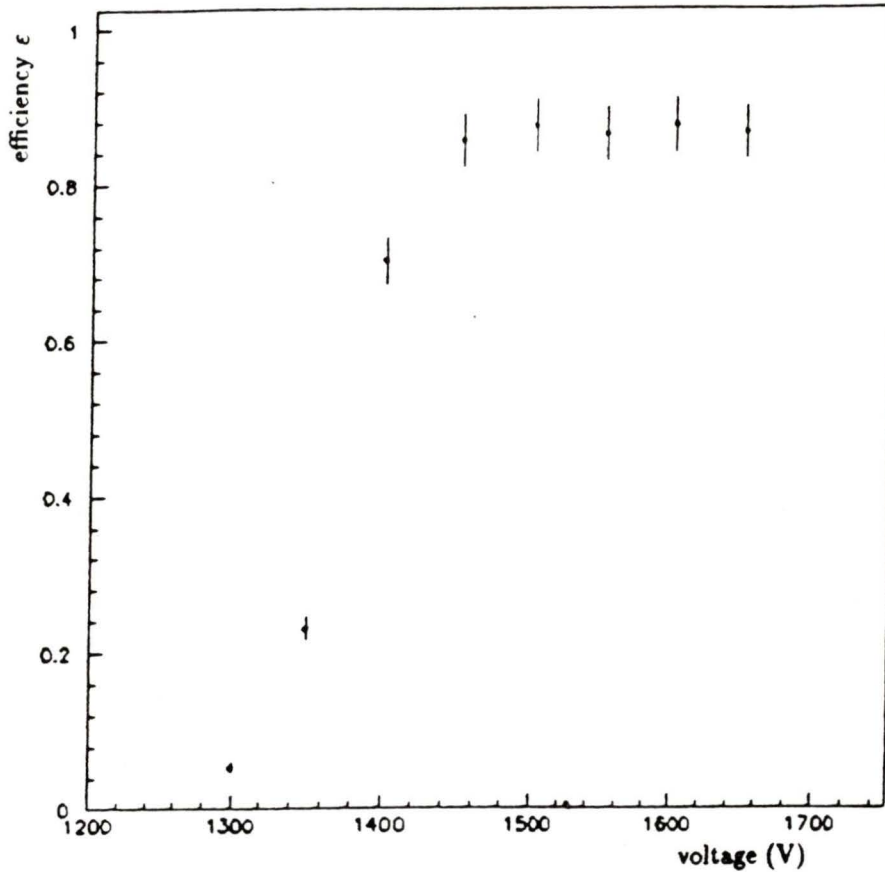


Figure 4.3: Plateau of counters

In order to reduce accidental coincidences and missed events due to the different delays of the signal cables, the pulse widths of the discriminators were carefully adjusted with the aid of an oscilloscope. The width of the pulses was chosen to be about 50ns.

The timing of the counters was checked by measuring the coincident rate as a function of delay time. The signal from one of the counters was

chosen as a zero time base and the signal from another counter was passed through a delay module. The signals were sent to a coincidence unit whose output was sent to scaler. The delay time was varied and the coincidences maximized in order to choose the best timing.

### 4.2.2 Event Selection by the Telescope

Cosmic rays at sea level are classified according to their energy, somewhat arbitrarily, into two categories. Those cosmic rays which are energetic enough to penetrate  $167 \text{ g/cm}^2$  of lead are classified as the "hard" component, all others as the "soft" component [29]. For muons, the hard component represents those muons above 220 Mev kinetic energy. Since there were approximately three meters of concrete lying above the experiment (the experiment was carried out in a basement laboratory) only hard cosmic rays could reach the test cell, the soft cosmic rays ranging out in the concrete. Among the hard cosmic rays, muons comprise the vast majority. The proton component peaks at less than 4% at 700 MeV, falling to an even lower percentage at energies both above and below 700 MeV. The pion component is even lower [30]. To good approximation we can thus consider the cosmic rays in this experiment exclusively as muons.

Event selection was accomplished by requiring a coincidence of all three telescope counters to trigger the data acquisition. A pile of iron absorber plates of total thickness 15.6 cm was placed between counter 2 and counter 3 in order to eliminate the low momentum cosmic rays, thus ensuring a pure Landau distribution in the energy loss spectrum. The minimum kinetic energy of muons passing through the test cell that could trigger the data acquisition was calculated by the Bethe Bloch formula as

$$E_{min} = 235 \text{ MeV}. \quad (4.3)$$

For this energy, the Landau parameter is

$$k = 0.0076, \quad (4.4)$$

so the data are expected to have a Landau distribution.

### 4.2.3 Estimation of Event Rate

The event rate for our cosmic ray telescope is given by

$$R = kIA\Omega, \quad (4.5)$$

where  $I$  is the flux of hard cosmic rays at sea level in the vertical direction,  $A$  is the sensitive detection area of the cell,  $\Omega$  is the solid angle of acceptance of the telescope, and  $k$  is the fraction of cosmic rays which have an energy appropriate to trigger our telescope.

From the geometry of the telescope, the area  $A$  and solid angle  $\Omega$  are approximately determined by the top and bottom scintillator  $S_1$  and  $S_3$

$$\Omega = \int \int_{S_3} \int \int_{S_1} \frac{\cos\theta}{L^2} dS_1 dS_3, \quad (4.6)$$

where  $dS_1$  and  $dS_3$  are the area elements of scintillator 1 and 3 respectively,  $L$  is the distance between the two elements, and  $\theta$  is the angle between the line connecting the two elements and the  $Z$  axis (see fig 4.4).

From fig 4.4, we have following relations:

$$\cos\theta = \frac{D}{L}, \quad L = \sqrt{l^2 + D^2}, \quad (4.7)$$

$$l^2 = (r\sin\phi - r'\sin\phi')^2 + (r\cos\phi - r'\cos\phi')^2,$$

$$dS_1 = r'dr'd\phi', \quad dS_3 = rdrd\phi,$$

where the constant  $D$  is the distance between the two scintillators.

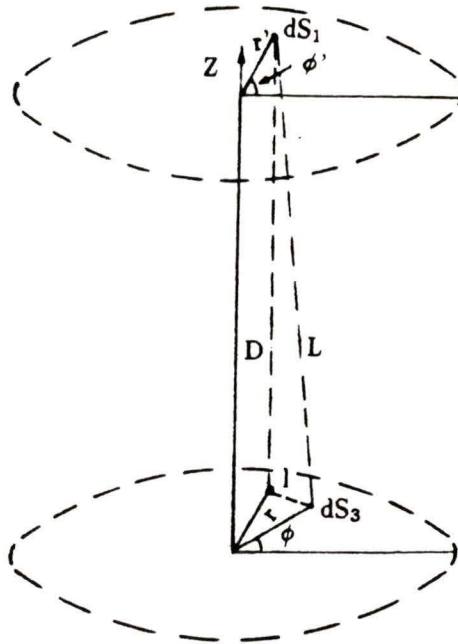


Figure 4.4: Solid Angle

The integration was done by Gaussian quadrature. For  $D = 33.6\text{cm}$ , we calculate

$$\Omega = 0.06833 \text{ sterad.} \quad (4.8)$$

The ratio  $k$  was calculated by a Monte Carlo program, using the muon momentum density distribution at sea level [31], shown in fig 4.5. The approximately three meter thickness of concrete above the telescope was included in the calculation. The result is

$$k = \frac{2}{3}. \quad (4.9)$$

The vertical flux of hard cosmic rays at sea level is about  $8 \times 10^{-3} \text{ cm}^{-2}\text{s}^{-1}\text{sterad}^{-1}$  [32], and  $A$  is approximately the area of  $S1$ . The above

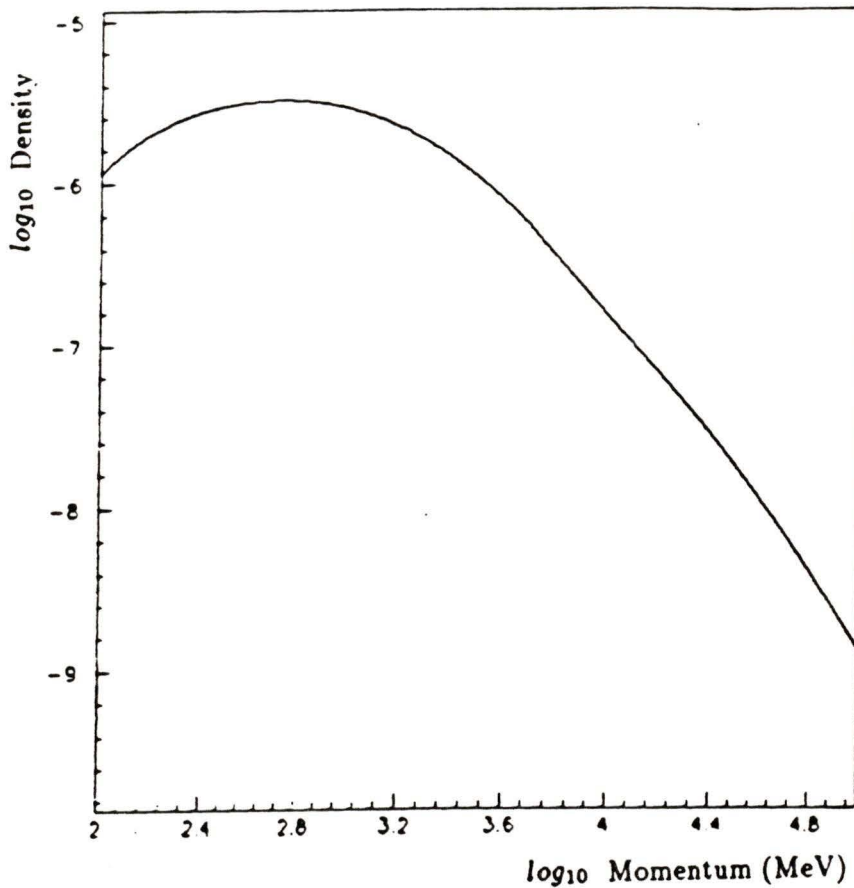


Figure 4.5: Muon momentum density distribution at sea level

results lead to an event rate

$$R = \frac{2}{3} \times 8 \times 10^{-3} \times 1.55^2 \pi \times 0.0683 = 2.75 \times 10^{-3}/s = 238/day. \quad (4.10)$$

In fact, we had about 240 events per day, in good agreement with the prediction.

### 4.2.4 Mean Path of Triggering Muon in TMP

Because triggering muons can penetrate the cell at different angles allowed by the telescope geometry, the mean path length of muons through the cell is a little longer than 1 cm. This mean path length must be known in order to calculate the most probable energy loss of muons in the test cell. The distribution of path lengths was simulated by the Monte Carlo method, taking account of the  $\cos^2\theta$  distribution of the incident cosmic ray flux. The result is

$$\bar{d} = 1.0044 \text{ cm.} \quad (4.11)$$

The distribution is shown in fig 4.6.

## 4.3 The Electronics System

### 4.3.1 Arrangement of Electronics

The experimental electronics system included a linear analog amplifier circuit, a logical trigger circuit, a digital data acquisition system, and a high voltage source and filters. After a particle penetrated the cell and cosmic ray telescope, a current pulse was generated in the linear circuit connected to the cathode of the cell. The signal from the test cell was first fed into a charge sensitive preamplifier<sup>1</sup>. The output from the preamplifier was then fed into a timing filter amplifier (TFA)<sup>2</sup>, set with a gain of 8 and with integration and differentiation out. The high pass characteristic of the TFA was used to help reduce the noise due to microphonics. Finally, the analog voltage output of the TFA was sent to a digital storage oscilloscope<sup>3</sup>, which received its trigger

---

<sup>1</sup>Tennelec TC 170, modified to be DC coupled and to have an input capacitance of approximately 5.pf

<sup>2</sup>Ortec model 474

<sup>3</sup>Tektronix 2440

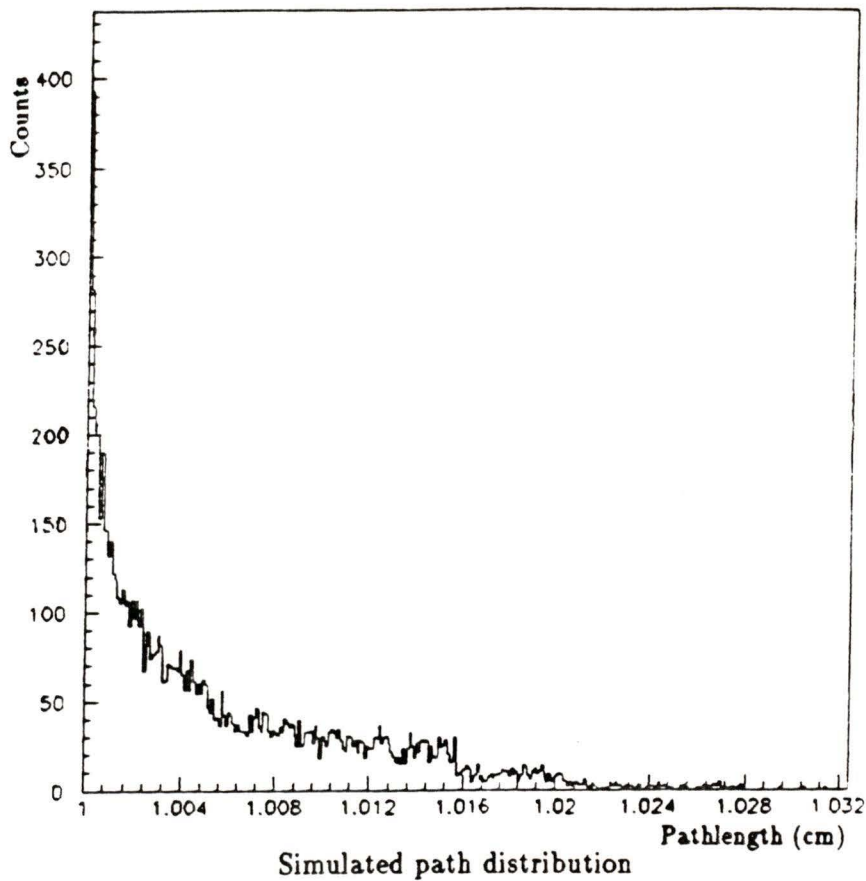


Figure 4.6: Distribution of path in TMP

from the cosmic ray telescope. A schematic of the electronics is shown in fig 4.7.

Positive high voltage (HV) was supplied to the anode of the test cell by a high voltage supply <sup>4</sup> and monitored by a digital voltmeter<sup>5</sup>. Since the test cell is essentially a capacitor, the ripple in the HV causes fluctuations of charge on the electrodes, so the instability of the HV source is a noise source in the waveform measurement. Hence, a very stable high voltage source is

---

<sup>4</sup>Bertan model 380X

<sup>5</sup>Fluke model 23

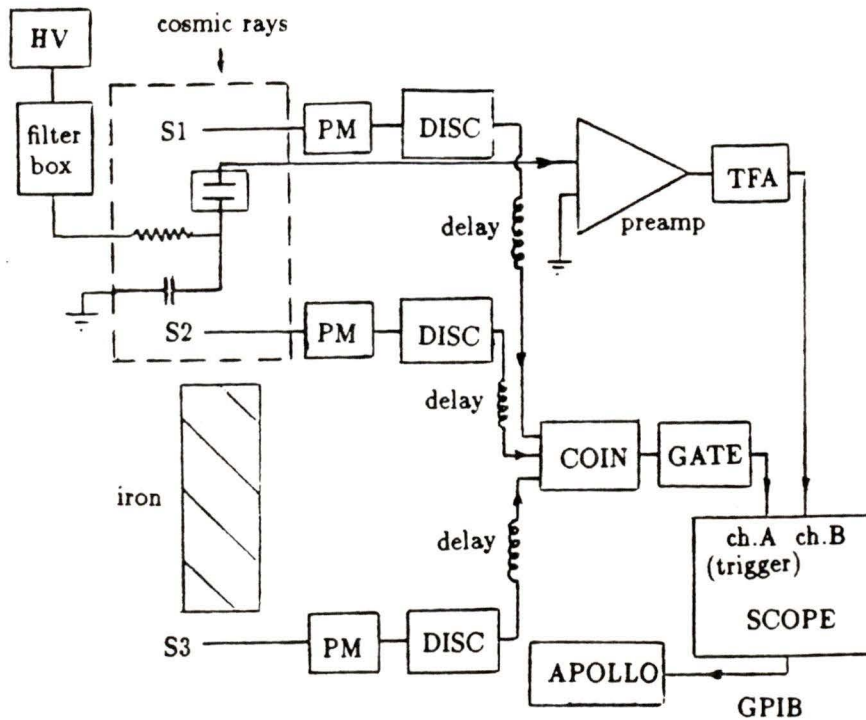


Figure 4.7: Arrangement of electronics

required. A low pass filter with 50 ms time constant, which smooths the voltage level efficiently, was placed between the HV source and the Faraday cage, and another low pass RC integrating filter of 53 ms time constant was located inside the cage for this purpose.

### 4.3.2 Data Acquisition System

The digital oscilloscope, controlled by a personal computer (PC) in the backplane of an APOLLO workstation<sup>6</sup>, was used as the data acquisition system. The analog signal  $v(t)$  from the amplifier system was digitized by

<sup>6</sup>Domain series 3500, Apollo Computer Inc..

an ADC in the oscilloscope. The total time base region of the oscilloscope is divided into  $2^{10} = 1024$  bins, and the voltage dynamic range is divided into  $2^8 = 256$  bins. After several tests, we set the total time base to  $204.8 \mu s$  and the dynamic range to  $102.4 \text{ mv}$ . The trigger point, on which the pulse rises, was set at  $1/4$  of the time axis, approximately  $51 \mu\text{sec}$ . In order to cover the negative pulse, the zero volt baseline level was set close to the top bin.

The digitized waveform was transferred to the PC in the backplane of the APOLLO for storage and later analysis.

### 4.3.3 Impulse Response of the System

The response  $h(t)$  of any linear electronic system to a delta function  $\delta(t)$  input is called the impulse response of the system. The output  $v(t)$  of an electronics amplifier system with impulse response  $h(t)$  is then the convolution of the input current  $i(t)$  with  $h(t)$

$$v(t) = \int_0^t i(\theta)h(t - \theta)d\theta. \quad (4.12)$$

The electronics chain for this experiment included a preamplifier and a timing filter amplifier. The timing filter amplifier can be idealized as an RC integrator and an RC differentiator. The charge sensitive preamplifier can be idealized as an integrating amplifier with a DC feedback resistor  $R$  in parallel with the feedback capacitor  $C$  (see fig 4.8).

The impulse response functions for an RC integrator, an RC differentiator, and an integrating amplifier can be derived using Laplace Transforms [36]:

a) The loop equation for the RC integrator in fig 4.8 is

$$\frac{V_i}{R + 1/SC} = \frac{V_o}{1/SC}, \quad (4.13)$$

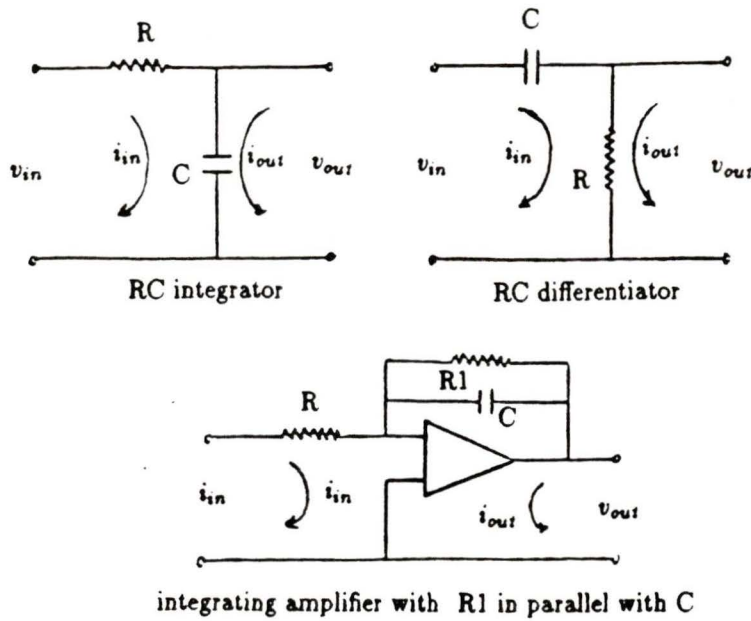


Figure 4.8: Idealized electronic chain

where  $S = i\omega$  and  $\omega$  denotes the angular frequency. The Laplace transfer function is therefore

$$\frac{V_o}{V_i} = \frac{1/SC}{R + 1/SC} = \frac{1/RC}{1/RC + S} = \frac{1/\tau}{1/\tau + S}, \quad (4.14)$$

where  $\tau \equiv RC$  is known as the RC time constant. The impulse response is then

$$h_i(t) = L^{-1}\left[\frac{1/\tau}{1/\tau + S}\right] = \frac{1}{\tau}e^{-t/\tau}. \quad (4.15)$$

b) The loop equation for the RC differentiator in fig 4.8 is

$$\frac{V_i}{R + 1/SC} = \frac{V_o}{R}, \quad (4.16)$$

so the Laplace transfer function is

$$\frac{V_o}{V_i} = \frac{R}{R + 1/SC} = \frac{RSC}{1 + RSC} = \frac{S\tau}{S\tau + 1}, \quad (4.17)$$

and the impulse response is

$$h_d(t) = L^{-1}\left[\frac{S\tau}{S\tau + 1}\right] = L^{-1}\left[1 - \frac{1/\tau}{1/\tau + S}\right] = \delta(t) - \frac{1}{\tau}e^{-t/\tau} \quad (4.18)$$

c) The loop equation for the integrating amplifier with DC feedback resistor  $R_1$  in parallel with  $C$  in fig 4.8 is

$$\frac{V_i}{R} + \frac{V_o}{(1/R_1 + SC)^{-1}} = 0, \quad (4.19)$$

so the Laplace transfer function is

$$\frac{V_o}{V_i} = \frac{-1/RC}{1/R_1C + S} = \frac{-1/\tau}{1/\tau_1 + S}. \quad (4.20)$$

Note however that the loop equation for an integrating amplifier with no DC feedback resistor  $R_1$  in parallel with  $C$  is

$$\frac{V_i}{R} + \frac{V_o}{1/SC} = 0, \quad (4.21)$$

so its Laplace transfer function is

$$\frac{V_o}{V_i} = \frac{-1}{RCS} = \frac{-1}{\tau S}, \quad (4.22)$$

and its impulse response is

$$h_a(t) = L^{-1}\left[\frac{-1}{\tau S}\right] = -\frac{1}{\tau}u(t), \quad (4.23)$$

where  $u(t)$  is the unit step function. The Laplace transfer function for an integrating amplifier with no DC feedback resistor (time constant  $\tau = RC$ ) in series with an RC differentiator (time constant  $\tau_1 = R_1C$ ) is the product of the two individual transfer function (4.17) and (4.22):

$$\frac{V_o}{V_i} = \left(\frac{-1}{\tau S}\right)\left(\frac{S\tau_1}{S\tau_1 + 1}\right) = \frac{-1/\tau}{1/\tau_1 + S}, \quad (4.24)$$

which can be seen is identical to the transfer function of the integrating amplifier with DC feedback resistor  $R_1$  in parallel with  $C$  (equation (4.20)). The preamplifier can thus be treated as an integrating amplifier (without DC feedback resistor  $R_1$ ) in series with an RC differentiator circuit.

The impulse response of equation (4.23) assumes an input voltage, whereas we have an input current. The input voltage is simply

$$v_{in}(t) = i_{in}(t)R, \quad (4.25)$$

so we can write

$$v_{out}(t) = \int_0^t v_{in}(\theta)h_a(t - \theta)d\theta = \int_0^t i_{in}(\theta)Rh_a(t - \theta)d\theta. \quad (4.26)$$

The current impulse response of the integrating amplifier (with no DC feedback resistor) then should be

$$H_a(t) = Rh_a(t) = -\frac{R}{\tau}u(t) = -\frac{R}{RC}u(t) = -\frac{1}{C}u(t). \quad (4.27)$$

Since our system can be idealized as an RC integrator, two RC differentiators, and an integrating amplifier (all in series), the impulse response of the entire electronics chain is just the convolution of the individual impulse responses. Their order does not affect the result. We can thus derive the

impulse response of the system by starting with an impulse current and then calculating the convolution step by step. After the impulse current passes the integrating amplifier, the voltage output is just  $H_a(t)$

$$v_{out} = \begin{cases} 0 & \text{for } t < 0 \\ -1/C & \text{for } t \geq 0. \end{cases}$$

This voltage is then passed through the integrator with a time constant  $\tau_1$ , and its output is

$$\begin{aligned} v_{out1} &= \int_0^t v_{out}(\theta) h_i(t - \theta) d\theta \\ &= -\frac{1}{C}(1 - e^{-t/\tau_1}). \end{aligned}$$

This voltage passes now through the first differentiator with a time constant  $\tau_2$ , and generates an output

$$\begin{aligned} v_{out2} &= \int_0^t v_{out1}(\theta) h_d(t - \theta) d\theta \\ &= \frac{1}{C}(e^{-t/\tau_1} - e^{-t/\tau_2}) - \frac{\tau_1}{C\tau_2(\tau_1 - \tau_2)}(e^{-t/\tau_1} - e^{-t/\tau_2}). \end{aligned}$$

This voltage is finally passed through the last differentiator with a time constant  $\tau_3$ , and the final output is given by

$$\begin{aligned} R(t) &= \int_0^t v_{out2}(\theta) h_d(t - \theta) d\theta \quad (4.28) \\ &= \frac{G\tau_2\tau_3}{C} \left( \frac{e^{-t/\tau_1}}{(\tau_1 - \tau_2)(\tau_1 - \tau_3)} + \frac{e^{-t/\tau_2}}{(\tau_2 - \tau_1)(\tau_2 - \tau_3)} + \frac{e^{-t/\tau_3}}{(\tau_3 - \tau_1)(\tau_3 - \tau_2)} \right), \end{aligned}$$

where we have included the factor  $G$  representing the gain of the timing filter amplifier.

In order to determine the time constants of equation (4.28) relevant to our system, an impulse current was put into the front end of the electronics chain and the output measured. The impulse current was generated by putting a voltage step  $V_{step}$  into the capacitor  $C_{test}$  of the preamplifier's test input:

$$i(t) = \frac{V_{step}}{C_{test}} \delta(t). \quad (4.29)$$

The output voltage was digitized by the digital storage oscilloscope, and then sent to the PC for storage and later analysis.

Since the differentiating time is much longer than the integrating time for our amplifier chain, we took two sets of impulse response function data. One was a slow speed sweep set with total time base of 1024  $\mu$  second which covers the total pulse. This set however cannot give accurate information about the shortest time constant in  $R(t)$ , because the integration time region only occupies one bin. Another data set with a total time base of 0.4096  $\mu$  sec was thus taken to expand the short integration time region and so capture the details of the fast rise of the pulse. For each set, we measured 1000 pulses and calculated the average waveform in order to acquire good statistics. We used the program MINUIT [33] as a least squares fitting routine to fit simultaneously the two sets of data to equation (4.28). The total  $\chi^2$  (chi-squared) of  $n$  data points

$$\begin{aligned} \chi^2 = & \sum_{i=1}^n (R(t_i)_{theory} - (R(t_i)_{exp.(1)} - back_{ave.(1)}))^2 / variance(1)^2 \\ & + \sum_{i=1}^n (R(t_i)_{theory} - (R(t_i)_{exp.(2)} - back_{ave.(2)}))^2 / variance(2)^2 \end{aligned} \quad (4.30)$$

was minimized, where  $back_{ave.(i)}$  is the average level of each pretrigger region,

i.e., the region before the rise of the pulse:

$$back_{ave.} = \frac{1}{m} \sum_{i=1}^m back(t_i). \quad (4.31)$$

The variance for each pulse was estimated from the spread of data in each pretrigger region, which is an estimate of the noise:

$$variance^2 = \frac{1}{m-1} \sum_{i=1}^m (back(t_i) - back_{ave.})^2. \quad (4.32)$$

Since the fast-sweep data suffered from some high frequency ringing which could not be incorporated into our model (and which was irrelevant to our experiment since the frequency of the ringing was well away from the frequency domain of the test cell current measurements) the variance for the fast-sweep data was artificially increased by a factor of 2.5 in order not to corrupt the fit of the slow-sweep time constants in the simultaneous fit.

The results of the simultaneous fit of the two data set are summarized in table 4.1. The parameters  $t_0$  are the trigger points, i.e., the start time for each pulse.

parameter	value	total error
TFA integration time $\tau_1 \mu s$	0.0140	0.0016
TFA differentiation time $\tau_2 \mu s$	284.8	24.0
Preamp differentiation time $\tau_3 \mu s$	20010.8	210.0
slow sweep speed $t_0 \mu s$	257.96	0.0012
fast sweep speed $t_0 \mu s$	0.16423	0.00011
G/C (DL/ $Q_{test}$ )	127.84	0.042
$\chi^2/d.o.f.$	1.52	

Table 4.1: Results of impulse function fit

The two pulses, along with the overlaid fit, are shown in figs 4.9 and 4.10. Systematic errors in the fit were estimated by holding  $\tau_1$  fixed to the

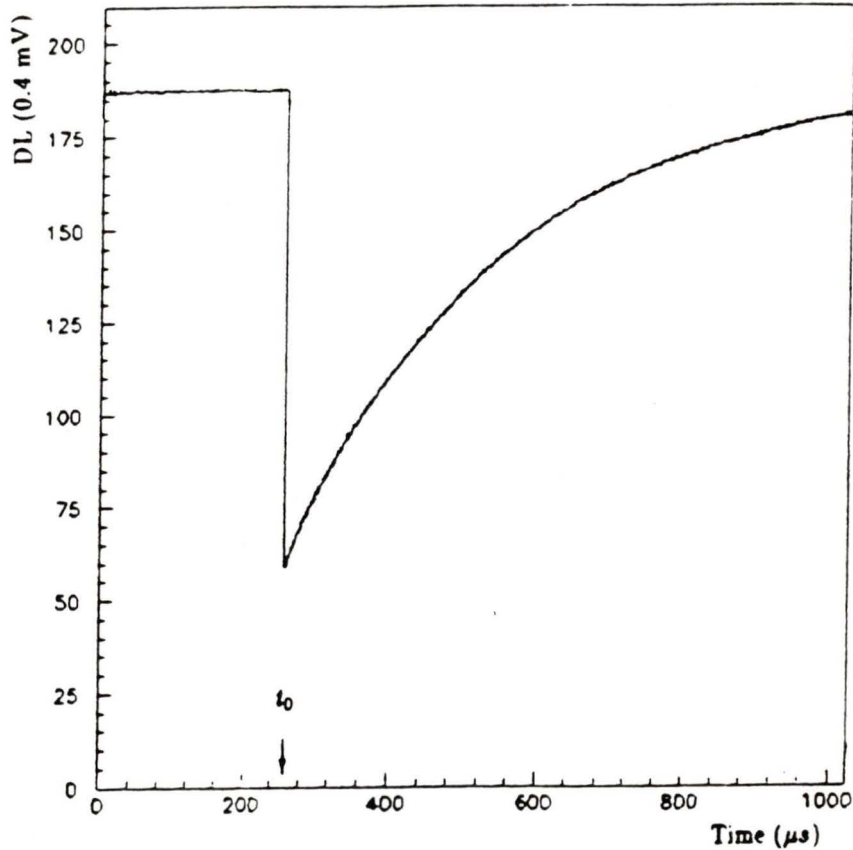


Figure 4.9:  $R(t)$ : data and fitted curve (slow sweep)

above value in a fit for  $\tau_2$  and  $\tau_3$  of the slow sweep data only, and by holding  $\tau_2$  and  $\tau_3$  fixed to above values in a fit for  $\tau_1$  of the fast sweep data only. The total error quoted in table 4.1 is the quadratic sum of the systematic and statistical errors. The statistical errors are the dominant errors, being a factor of 3.8 or more greater than the systematic errors.

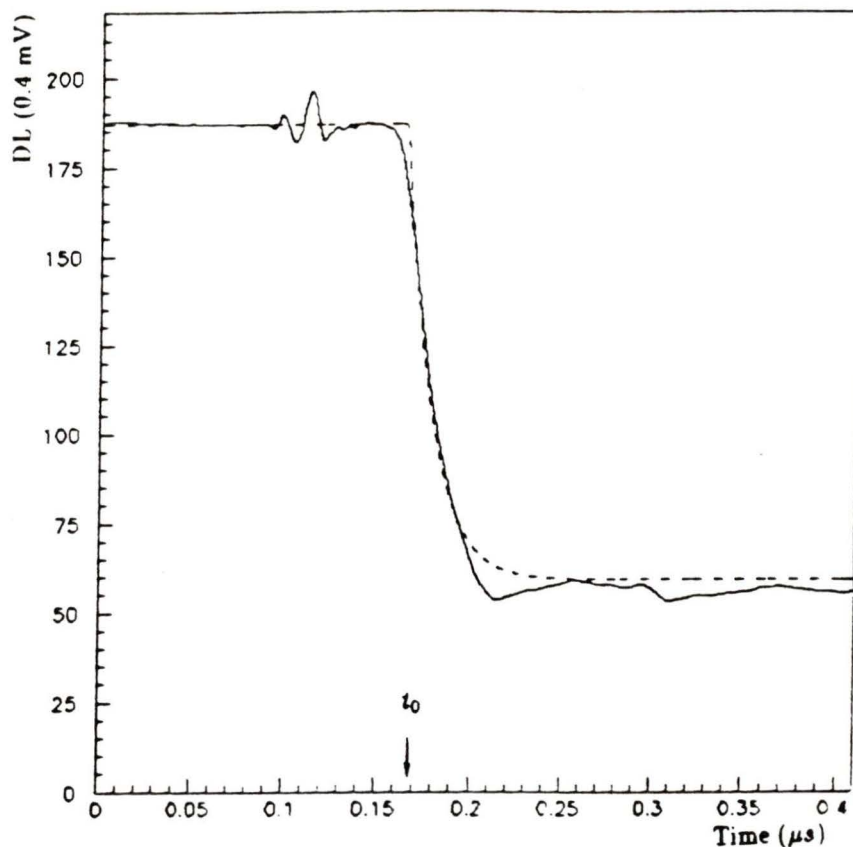


Figure 4.10:  $R(t)$ : data and fitted curve (fast sweep)

#### 4.3.4 Charge Sensitivity

If the test capacitance of the preamplifier had been sufficiently well known, the charge sensitivity of the electronics chain could have been determined from the impulse response measurement of the previous section. The test capacitance was however not sufficiently well known, so the charge sensitivity had to be determined by a separate measurement. The measurement was similar to the previous procedure, except that a measured capacitor was used rather than the test capacitor of the preamplifier. A known charge  $Q_{test}$  was

then produced by putting a voltage step  $V_{in}$  into the measured capacitor  $C_m$  which was coupled to the input of the preamp. The value of the charge  $Q_{test}$  is then simply

$$Q_{test} = C_m V_{in}. \quad (4.33)$$

In order to minimize the uncertainty in charge sensitivity due to the uncertainty in capacitance  $C_m$ , we did 9 measurements with different  $C_m$ 's ranging in value from 4.7 pf to 6.8 pf. In each measurement, 256 input pulses  $V_{in}(t)$  and output pulses  $V_{out}(t)$  were recorded and averaged for good statistics.

The input pulse was fitted to a step function to get  $V_{in}$ , and the output pulse was fitted to the impulse response function with time constants fixed at the values obtained in the last section to get G/C in units of DL/ $Q_{test}$ , where DL stands for "digitization levels". The results of the fitted  $V_{in}$  and G/C, and the measured  $C_m$  are shown in table 4.2.

trial	$V_{in}$ ( $\mu V$ )	$C_m$ (pF)	$Q_{test}$ (electrons)	G/C ( $\frac{DL}{Q_{test}}$ )
1	$390.18 \pm 0.03$	5.85	$14248 \pm 487$	$125.71 \pm 1.51$
2	$424.70 \pm 0.35$	5.85	$15509 \pm 530$	$124.36 \pm 1.49$
3	$432.06 \pm 0.88$	5.775	$15575 \pm 540$	$122.69 \pm 1.47$
4	$501.02 \pm 0.55$	5.3	$16576 \pm 626$	$126.09 \pm 1.51$
5	$508.24 \pm 0.84$	4.85	$15387 \pm 635$	$123.20 \pm 1.48$
6	$582.44 \pm 0.85$	4.55	$16542 \pm 728$	$127.87 \pm 1.54$
7	$366.52 \pm 0.59$	6.975	$15958 \pm 458$	$122.52 \pm 1.48$
8	$363.02 \pm 0.85$	6.775	$15352 \pm 455$	$124.67 \pm 1.50$
9	$389.74 \pm 0.04$	6.775	$16482 \pm 487$	$123.35 \pm 1.48$

Table 4.2: Fitted results of input and output pulses

The error  $\sigma_C$  on each  $C_m$  was estimated to be 0.20 pf. The charge

$Q_{test}$ , in number of electrons, is given by

$$Q_{test} = \frac{C_m V_{in}}{e}, \quad (4.34)$$

where  $C_m$  and  $V_{in}$  are expressed in farads and volts respectively, and  $e = 1.602 \times 10^{-19}$  coulombs is the electron charge. The charge sensitivities for each of the nine different trials were calculated by

$$S = \frac{G/C(DL)}{Q_{test}(electrons)} \times 400.0 \frac{\mu V}{DL}. \quad (4.35)$$

where the factor of  $400.0 \mu V/DL$  represents one digitization level of the oscilloscope.

The results of the nine trials are listed in table 4.3 and shown in fig 4.11. The error on each measurement was estimated by combining the errors on each parameter of table 4.2.

trial	$S_i$ ( $\mu$ V/electron)	error $\sigma_i$
1	3.5291	0.1279
2	3.2074	0.1162
3	3.1509	0.1156
4	3.0427	0.1205
5	3.2027	0.1377
6	3.0919	0.1410
7	3.0710	0.0957
8	3.2482	0.1038
9	2.9934	0.0954

Table 4.3: The charge sensitivities

The weighted average of the individual entries of table 4.3 is taken as the charge sensitivity:

$$S = \frac{\sum_{i=1}^9 w_i S_i}{\sum_{i=1}^9 w_i} = 3.155 \mu V/electron, \quad (4.36)$$

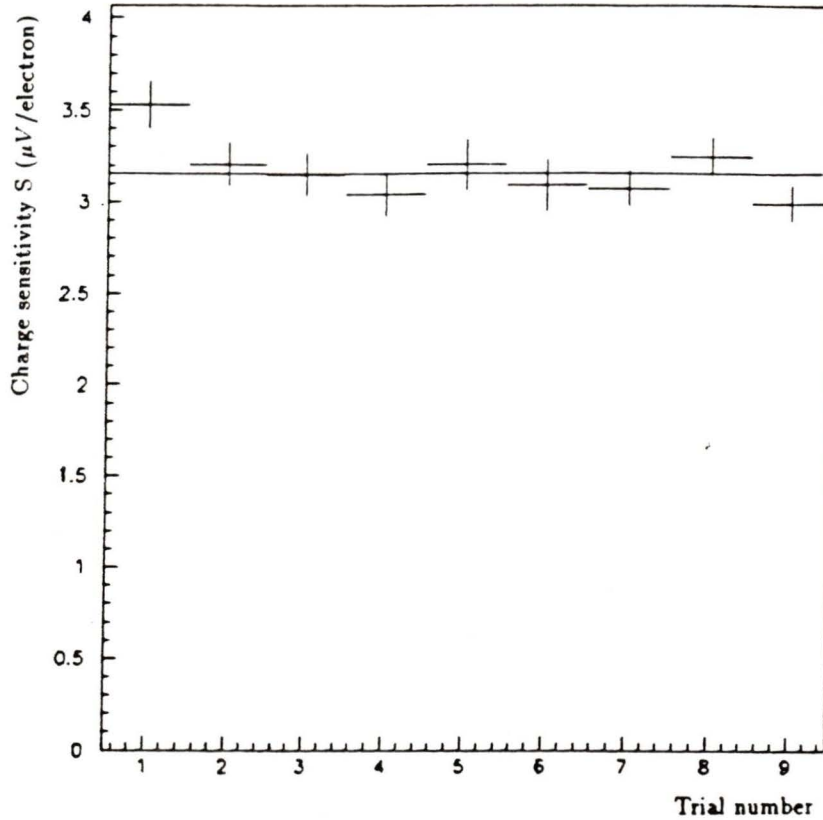


Figure 4.11: Measured charge sensitivities

where

$$w_i = 1/\sigma_i^2.$$

We take as the uncertainty in charge sensitivity the estimated full width at half maximum of the distribution of the nine individual measurements:

$$\sigma_S = 0.113 \mu V/electron.$$

Since our determination of free ion yield depends critically on the charge sensitivity measurements, which in turn depend on how well we measured the test capacitance, it was important to verify that the capacitance

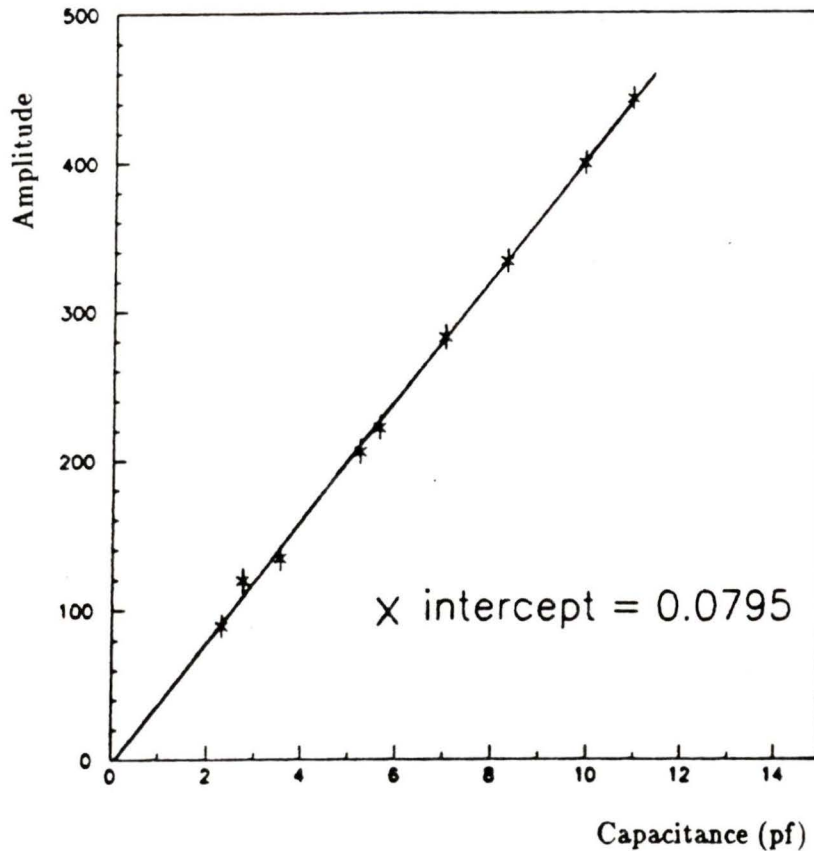


Figure 4.12: Capacitance as a function of amplitude

measurements were unbiased. To verify that our capacitance measurements were unbiased, we repeated the above procedure, this time keeping the input voltage step fixed at  $400 \mu\text{v}$  and using capacitors ranging in value from 2.2 pf to 12 pf. A straight line was then fitted to the resultant capacitance versus amplitude data (see fig 4.12), yielding a zero intercept of  $0.08 \pm 0.16$  pf. A zero intercept not consistent with zero would have indicated a bias in our capacitance measurements.

## Chapter 5

# The Mobility and Lifetime of Free Electrons

### 5.1 Theoretical Formula of Waveform

We use a waveform analysis to obtain the mobility and lifetime of free electrons in TMP. For a cosmic ray induced current  $i(t)$  on the cathode of the test cell, the theoretically expected shape of the waveform is the convolution of the current pulse with the impulse response function  $R(t)$  for the electronics:

$$v(t) = \int_0^t i(\theta)R(t - \theta)d\theta, \quad (5.1)$$

with the current of equation (2.26)

$$i(t) = \begin{cases} 0 & \text{for } t < 0, \\ \frac{Q_0(E)}{t_d} \left(1 - \frac{t}{t_d}\right) e^{-t/\tau} & \text{for } 0 \leq t \leq t_d, \\ 0 & \text{for } t > t_d. \end{cases}$$

Substituting  $R(t)$  from equation (4.28) and integrating, we have

$$v(t) = \begin{cases} 0 & \text{for } t < 0, \\ Q_0(E)S \sum c_i \left[ \left( \frac{t}{t_d} - 1 \right) e^{-t/\tau'_i} + \frac{\tau'_i}{t_d} (e^{-t/\tau'_i} - 1) + 1 \right] \frac{\tau'_i}{t_d} e^{-t/\tau'_i} & \text{for } 0 \leq t \leq t_d, \\ Q_0(E)S \sum c_i \left[ \frac{\tau'_i}{t_d} (e^{-t_d/\tau'_i} - 1) + 1 \right] \frac{\tau'_i}{t_d} e^{-t/\tau'_i} & \text{for } t > t_d, \end{cases} \quad (5.2)$$

where

$$\frac{1}{\tau'_i} = \frac{1}{\tau_l} - \frac{1}{\tau_i},$$

and

$$c_i = \prod_{j=1, j \neq i}^3 \frac{\tau_j}{(\tau_i - \tau_j)}, \quad i = 1, 2, 3,$$

and where  $\tau_l$  is the electron life time,  $t_d$  is the electron drift time, and  $S$  is the charge sensitivity.

Since we know  $S$  and the three time constants  $\tau_i$ , by measuring  $v(t)$  at various field strengths and fitting the resulting pulse shapes to equation (5.2), we can extract the parameters  $Q_0(E)$ ,  $\tau_l$ , and  $t_d$ .

## 5.2 Noise, Data Acquisition, and Initial Cuts

There were two types of noise which dominated our measurements. One is a high frequency noise, or thermal noise, which is from the random motion of electrons in the circuit. The other one is low frequency, mainly from acoustical noise and from the instability of the high voltage source. Both types of noise are random, so that by averaging many pulses together the noise amplitude should approach zero. By observation of single pulses with the oscilloscope (fig 5.1), one can see that the amplitude of the low frequency

noise was much higher than that of the high frequency noise, and close to the amplitude of the signal. But for an average of 500 pulses (fig 5.4), the amplitude of the low frequency noise almost vanishes and the amplitude of the high frequency noise is also very small compared with the signal amplitude. Hence, the noise background can be approximated very closely as a constant level for the averaged waveform.

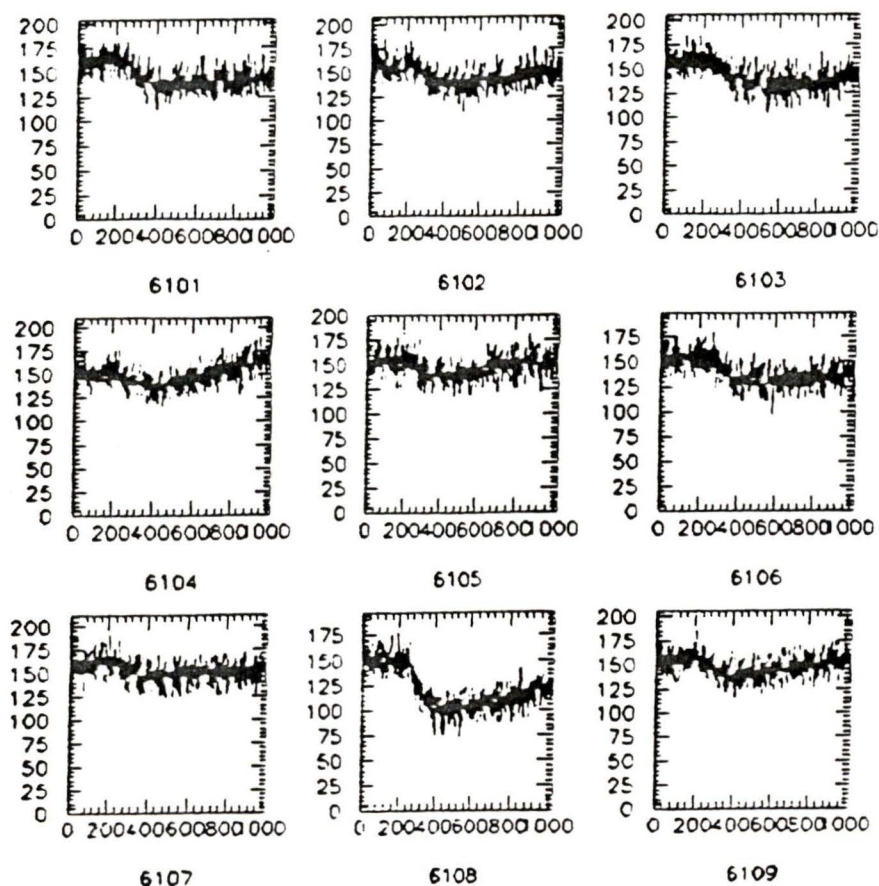


Figure 5.1: A sample of measured pulses

To measure  $t_d$  and the free ion yield at various electric field strengths, we set the high voltage on the test cell to 10 different values. For each voltage,

we measured 500 pulses. Before averaging them, we did initial quality cuts to discard data which saturated the digitizer, i.e., pulses which contained digitization levels of 0 or 255. Also cut from the data sample were false trigger events. These were determined by fitting a straight line through the data, with those having a variance less than 50 being cut (fig 5.2). The number of pulses surviving the cuts for each set of data is listed in table 5.1.

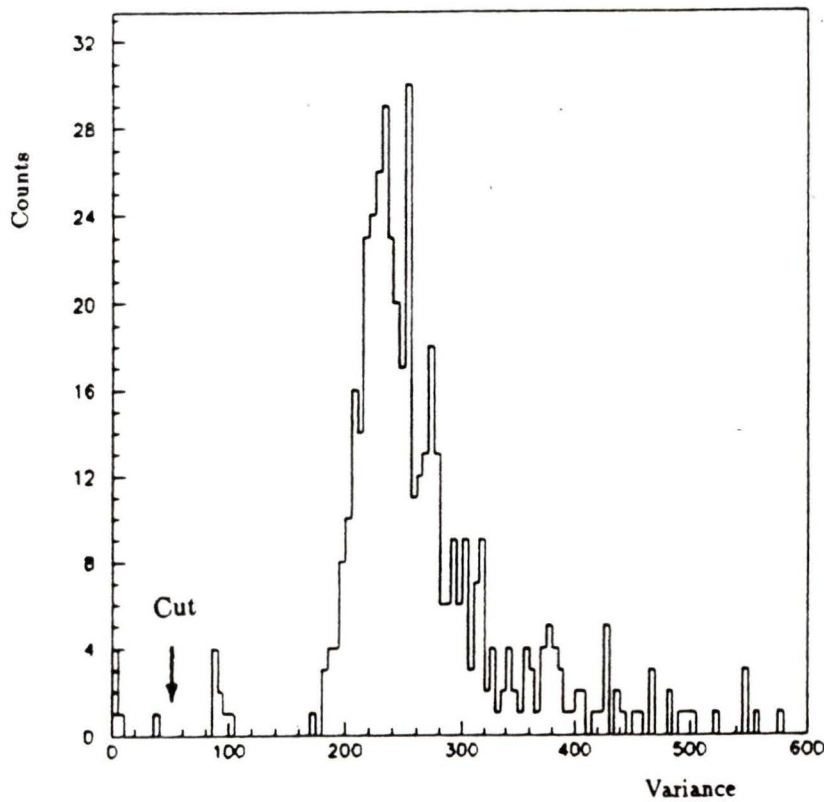


Figure 5.2: Variance with cut for 3.5 kV data

250v	500v	750v	1.0kv	1.5kv	2.0kv	2.5kv	3.0kv	3.5kv	4.0kv
499	497	492	498	488	495	492	481	465	471

Table 5.1: Number of pulses used at each high voltage

### 5.3 Fits

The ten averaged waveforms were fitted globally, i.e., all pulses were fitted simultaneously, using MINUIT [33], a least squares fitting program. MINUIT minimizes a function which we have defined as a total  $\chi^2$  to get the values of the parameters at the point of minimum  $\chi^2$ . The total  $\chi^2$  of  $n$  data points is given by

$$\chi^2 = \sum_{j=1}^{10} \sum_{i=1}^n (v_j(t_i)_{theory} - [v_j(t_i)_{experiment} - v_{j\ ave.}])^2 weight_i, \quad (5.3)$$

where  $j$  sums over the ten pulses and  $i$  sums over the time bins of each pulse. The average baselines  $v_{j\ ave.}$  for each averaged pulse were obtained by averaging the data of the 250 point pretrigger region of each pulse:

$$v_{j\ ave.} = \frac{1}{250} \sum_{i=1}^{250} v_j(t_i). \quad (5.4)$$

There are two contributions to the weight calculation. The main contribution is from the random electronic and acoustical noise discussed in section 5.2, which was estimated from the standard deviations of the constant level fits to the pretrigger regions:

$$error_1^2 = \frac{1}{249} \sum_{i=1}^{250} (v(t_i) - v_{ave.})^2. \quad (5.5)$$

The other contribution to the weight is a systematic error caused by the uncertainties in the time constants of the impulse response function. It

was estimated by the standard method of error propagation:

$$\begin{aligned} error_{2i}^2 &= (dv(t_i))^2 \\ &= \sum_{j=1}^3 \left( \frac{\partial v(t_i)}{\partial \tau_j} \right)^2 (d\tau_j)^2. \end{aligned} \quad (5.6)$$

The weight at time bin  $i$  then is given by

$$weight_i = \frac{1}{error_1^2 + error_{2i}^2}. \quad (5.7)$$

In the global fit, the voltage dependent drift time was expressed as

$$t_d = \frac{d^2}{\mu V}. \quad (5.8)$$

To justify the use of this expression in the global fit, we fixed the  $\tau_l$  and  $t_0$  at  $120 \mu s$  and  $51.2 \mu s$  respectively, estimated from a preliminary fit, then fitted the ten different  $t_d$ 's for each voltage. We then fitted a straight line to  $1/t_d$  as a function of  $V$ , with the fitted slope being an estimate of the mobility (see fig. 5.3). The result of the fit was  $\mu = 25.86 \pm 0.25 \text{ cm}^2 V^{-1} s^{-1}$  with a chi-squared per degree of freedom ( $\chi^2/dof$ ) = 1.5. The fact that  $1/t_d$  varies linearly with  $V$  verified that the electron mobility of TMP is independent of electric field strength at low field strengths.

There are thus a total of 13 free parameters in the global fitting program. They are the electron life time, the mobility, the trigger point, and each of the ten charge yields at the ten field strengths. The results of the global fit are summarized in table 5.2. Fig. 5.4 is a sample of a measured average waveform and the corresponding fitted curve.

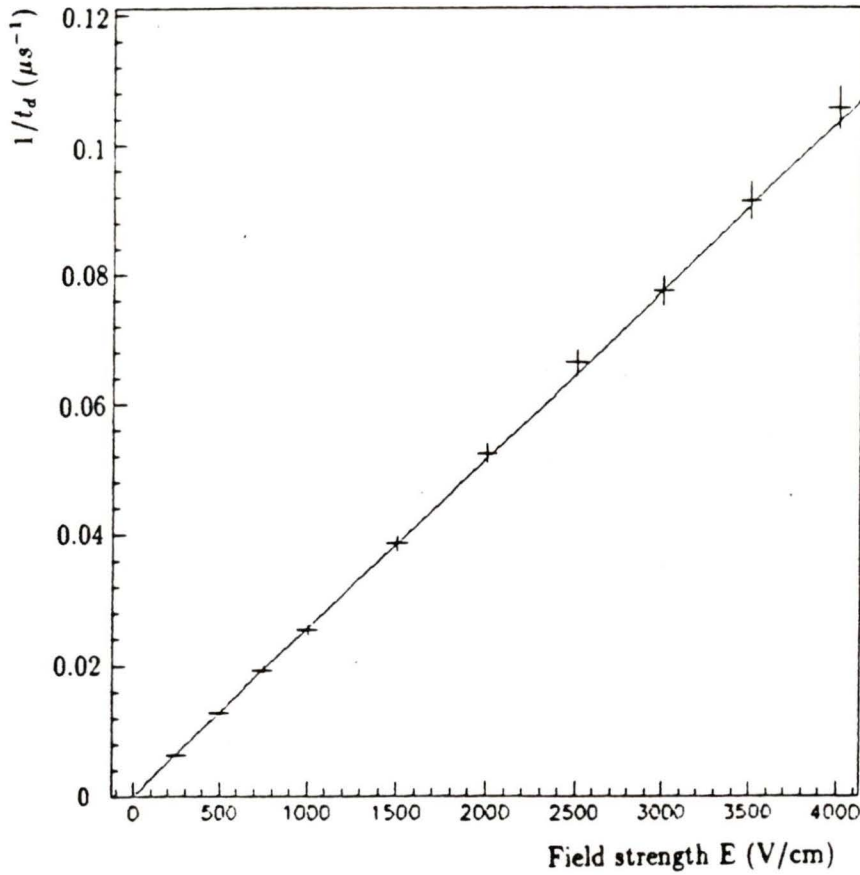


Figure 5.3:  $1/t_d$  as a function of field

## 5.4 Systematic Errors

The major source of systematic error in this analysis is due to the correlation between mobility and electron life time. In order to better understand the effects of these parameters on the pulse shapes, computer simulations of the pulse shapes were made, using our measured impulse response, at two different field strengths, and for various values of the ratio  $\tau_l/t_d$ . Plots of these simulations are shown in fig. 5.5 and 5.6. The dotted line in each of the two plots are simulations with  $\tau_l/t_d$  set to the value obtained in our

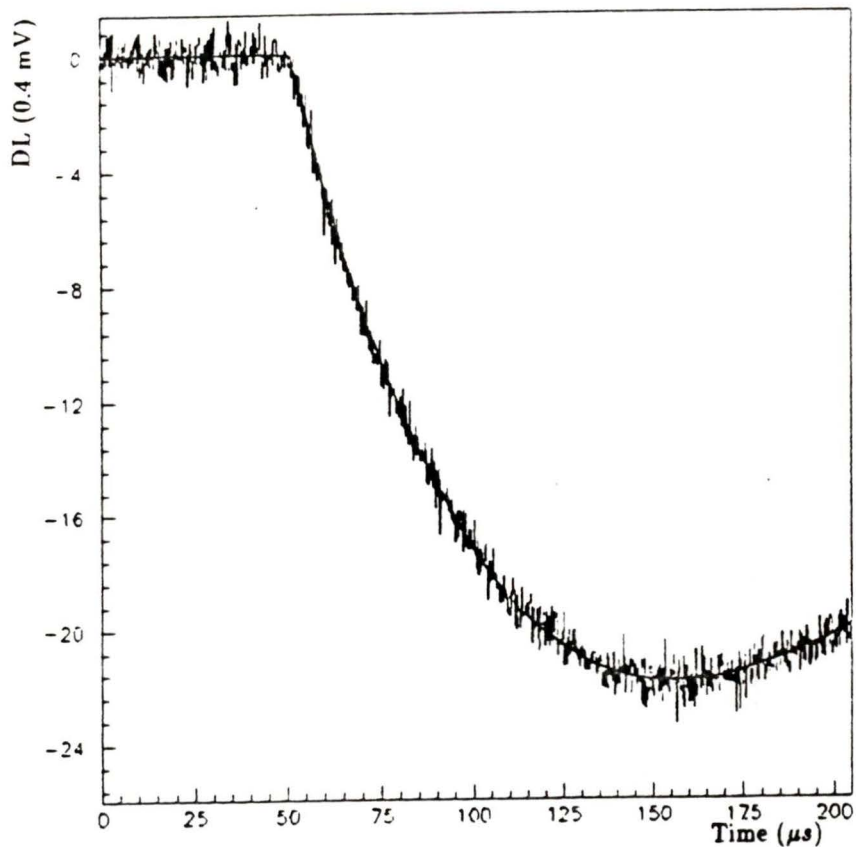


Figure 5.4: Average wave form and fitted curve at 250 V

global fit. The dashed line in the plots connects all the peak positions of the pulses, i.e., the points at which each pulse "turns over". It is evident from the plots that the pulse shape is most sensitive to  $\tau_l$  when  $\tau_l/t_d < 1$ , a condition apparently satisfied only with our 250 V data.

For a given  $t_d$ , the peak position is affected by both the electron life time  $\tau_l$  and the decay time of the electronics chain. Only with the 250 V data set, however, is the peak position made significantly earlier by finite electron life time effects. It can be seen also from fig. 5.5 that for pulses

parameter	value	statistic error
trigger point $t_0$ ( $\mu$ s)	51.155	0.007
life time $\tau_l$ ( $\mu$ s)	120.57	1.36
mobility $\mu$ ( $cm^2V^{-1}s^{-1}$ )	26.282	0.041
$Q_0(4.0kV)$ (electrons)	13219	6
$Q_0(3.5kV)$ (electrons)	12906	6
$Q_0(3.0kV)$ (electrons)	12870	6
$Q_0(2.5kV)$ (electrons)	12931	6
$Q_0(2.0kV)$ (electrons)	12285	5
$Q_0(1.5kV)$ (electrons)	12266	6
$Q_0(1.0kV)$ (electrons)	11441	6
$Q_0(750V)$ (electrons)	11721	7
$Q_0(500V)$ (electrons)	11344	8
$Q_0(250V)$ (electrons)	10518	12
$\chi^2/d.o.f.$	1.197	

Table 5.2: Results of global fitting

with  $\tau_l/t_d > 1$ ,  $Q_0$  starts to become correlated with  $\tau_l$  since more charge is collected as  $\tau_l$  is increased. It is evident from the figure however that it would require a large change in  $\tau_l$  to mimic even a few percent change in  $Q_0$ . It is only with the combination of data taken at various field strengths that we are able to unambiguously extract the values of  $Q_0$ ,  $\tau_l$  and  $t_d$ .

This is further illustrated in fig. 5.7, where we have plotted  $\mu$  versus fixed  $\tau_l$  for each averaged pulse (labeled by the corresponding voltage) as well as for the ten pulses simultaneously (labelled 'global'). The data for these plots was obtained by holding  $\tau_l$  fixed at various values and minimizing the  $\chi^2$  of equation (5.3) with respect to  $\mu$  (and  $Q_0$ ).  $t_0$  was held fixed at 51.155  $\mu$ sec for all these fits. It is again evident that the high field strength data has little sensitivity to  $\tau_l$ , whereas the 250 V data shows a high correlation between  $\tau_l$  and  $\mu$ , and only the combination of the various data sets allows an unambiguous determination of the parameters.

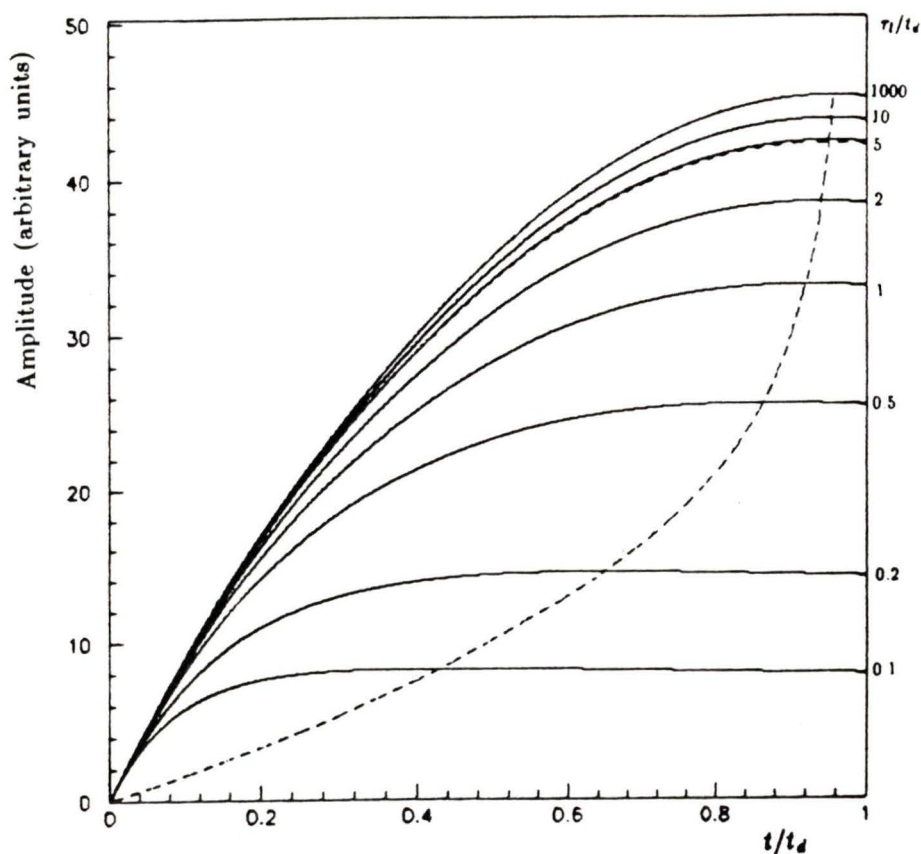


Figure 5.5:  $v(t)$  vs  $t/t_d$  for various  $\tau_l$  at 1000 V

The various aspects of the analysis discussed above are used as a guide in our strategy for determining systematic errors. Since the 250 V data is the most sensitive to  $\tau_l$ , we fit that data set alone, holding the mobility fixed at the value obtained in the global fit and allowing only  $\tau_l$ ,  $t_0$ , and  $Q_0$  to be free parameters. The value of  $\tau_l$  thus obtained was then held fixed in another global fit, allowing only  $\mu$ ,  $t_0$ , and the ten  $Q_0$ 's to be free parameters. Also examined was the effect of reducing the fitting window from the full 204.8  $\mu\text{sec}$  to  $1.1 t_d$  for each pulse, as well as fitting each pulse individually and

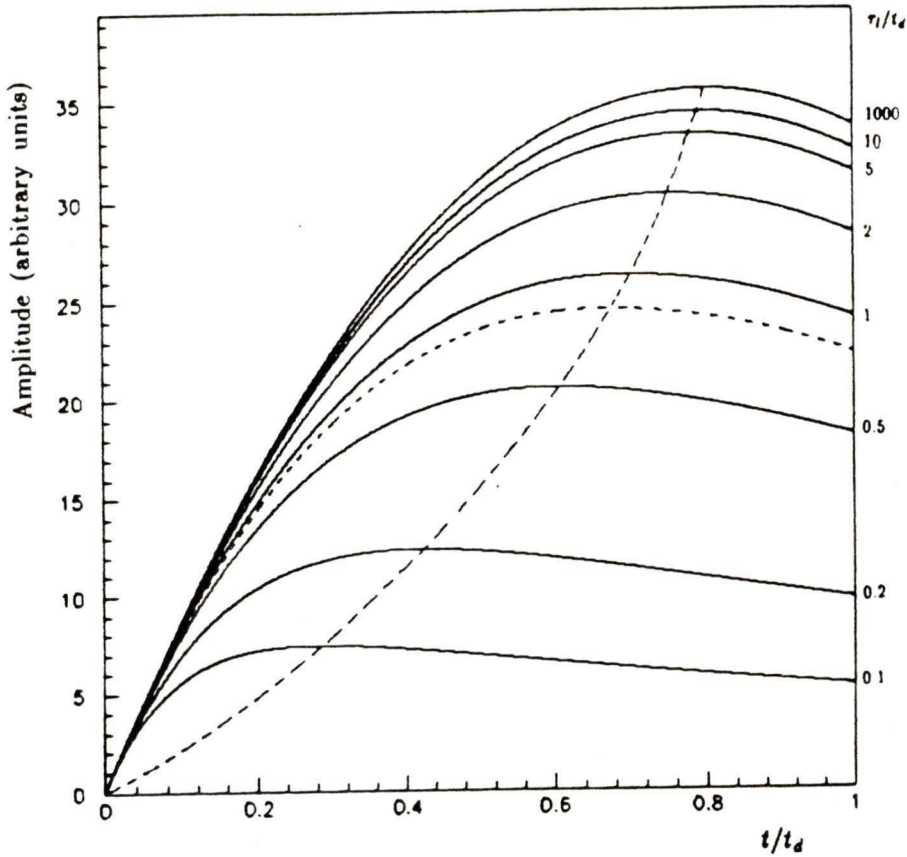


Figure 5.6:  $v(t)$  vs  $t/t_d$  for various  $\tau_1$  at 250 V

then calculating the weighted average of the various fitted parameters. The results of these fitting strategies are summarized in table 5.3. The differences between the central parameter values (obtained from the original global fit) and the extremes of values listed in table 5.3 are taken as the systematic fitting errors, i.e.,

$$\sigma_{\tau_1}(\text{systematic}) = \pm |139.3 - 120.6| = \pm 18.7 \mu\text{s},$$

and

$$\sigma_{\mu}(\text{systematic}) = \pm |26.909 - 26.282| = \pm 0.627.$$

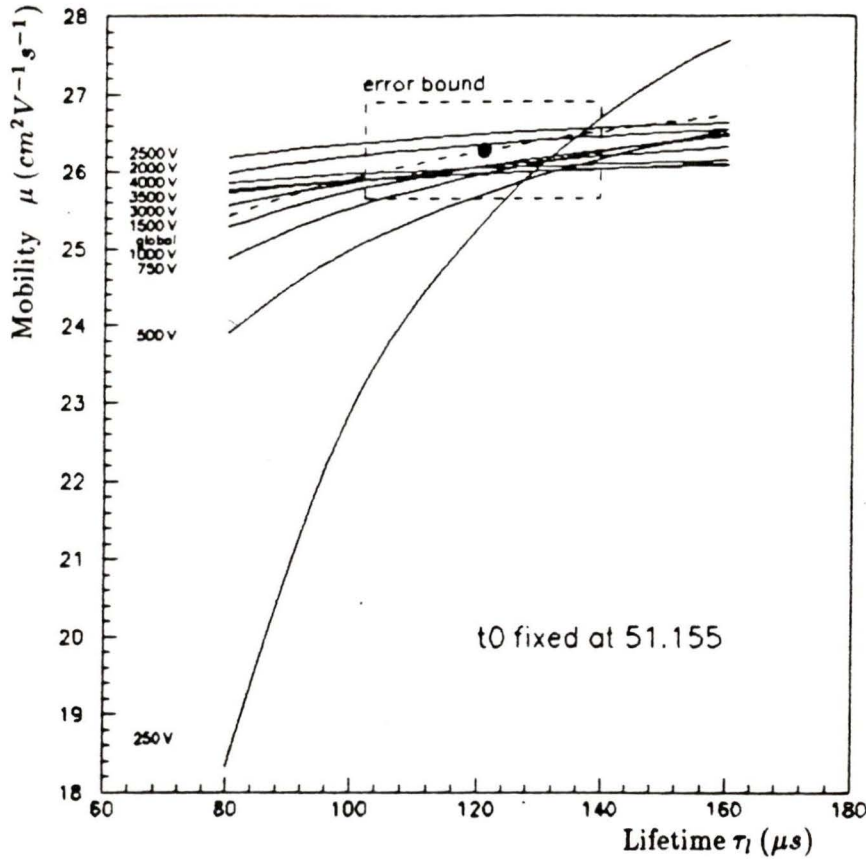


Figure 5.7:  $\mu$  vs  $\tau_l$  for various HV

These error bounds, added in quadrature to the statistical error bounds, are illustrated in fig. 5.7. The dot at the center of the bounds is the central value (from table 5.2).

Another systematic error to consider is the uncertainty in  $\mu$  due to the uncertainty in electrode spacing  $d$ . This can be determined by the standard method of error propagation:

$$\sigma_\mu = \sqrt{\left(\frac{\partial\mu}{\partial d}\right)^2\sigma_d^2} = \frac{2d}{t_d V}\sigma_d = 2\mu\frac{\sigma_d}{d} = 0.526 \text{ cm}^2\text{V}^{-1}\text{s}^{-1}. \quad (5.9)$$

	conditions	$\mu$	$\tau_l$	t0	$\chi^2/dof$
best=>	global fit, all chns	26.282	120.6	51.155	1.197
	global fit to 1.1 td	26.623	125.2	51.162	1.326
hi $\tau_l$ =>	250V data only	(26.282)	139.3	50.583	1.023
	250V data only	(26.282)	129.9	(51.155)	1.074
	global fit, all chns	26.585	(139.3)	51.173	1.215
hi $\mu$ =>	global fit to 1.1 td	26.909	(139.3)	51.173	1.352
lo $\mu$ =>	10 individual fit avg.	25.807	(120.6)	51.134	
	10 individual fit avg.	26.035	(120.6)	(51.155)	

Table 5.3: Summary of systematic error analysis. Parameter values in parentheses indicate that those parameters were held fixed in the fit.

Adding in quadrature the two systematic uncertainties in  $\mu$  results in

$$\sigma_{\mu}(\text{systematic}) = \sqrt{0.627^2 + 0.526^2} = 0.818 \text{ cm}^2\text{V}^{-1}\text{s}^{-1}. \quad (5.10)$$

Finally, we obtain

$$\tau_l = 120.6 \pm 1.4 \pm 18.7 \text{ } \mu\text{s},$$

and

$$\mu = 26.282 \pm 0.041 \pm 0.818 \text{ cm}^2\text{V}^{-1}\text{s}^{-1},$$

where the first error quoted for each is due to statistical effects and the second is due to systematic effects.

## Chapter 6

# Effect of Field on Free Ion Yield

### 6.1 Method to Measure $G_{fi}(E)$

The free ion yield per 100 eV deposited energy was expressed in equation (2.5):

$$G_{fi}(E) = 10^{-4} \frac{Q_0(E)}{\Delta}, \quad (6.1)$$

where  $Q_0(E)$  is the number of electrons liberated and  $\Delta$  is the energy deposited by the passing ionizing particle (in MeV). In principle, one could use the ten  $Q_0$ 's determined in the analysis of chapter 5 to estimate  $Q_0(E)$ . Those  $Q_0$ 's however are estimates of the mean number of freed electrons. Due to the combination of poor statistics and the asymmetry of the Landau distribution, the mean cannot be determined accurately in this experiment. Rather than using the mean, we will calculate the most probable number of freed electrons. This will be achieved for each field strength by fitting each individual pulse for  $Q_0$  only (keeping  $t_0$ ,  $\tau_1$  and  $\mu$  at their measured values),

then histogramming the results to form a pulse height distribution. The most probable number of freed electrons  $Q_0(E)_{mp}$  can then be easily determined from each pulse height distribution. Since our calculation of  $G_{fi}(E)$  will be based on the most probable number of freed electrons, the energy loss term in equation (2.5) must also be "most probable", so equation (2.5) can now be written

$$G_{fi}(E) = 10^{-4} \frac{Q_0(E)_{mp}}{\Delta_{mp}}. \quad (6.2)$$

## 6.2 Calculation of the Most Probable Energy Loss of Cosmic Ray Muons in the Test Cell

The most probable energy loss  $\Delta_{mp}$  in the Landau distribution is given by [24]

$$\Delta_{mp} = \xi[\ln(\xi/\varepsilon') + 1.98 - \delta], \quad (6.3)$$

where

$$\ln\varepsilon' = \ln[(1 - \beta^2)I^2/2m_e v^2] + \beta^2,$$

and  $\delta$  is known as the density effect correction. All other terms of equation (6.3) are defined in section 2.2. Details of the density effect correction are given in [34], and in particular for TMP in [35]. Since the cosmic ray flux is not monoenergetic, but rather falls as  $E^{-2}$  for energies above a few hundred MeV [31], the most probable energy loss for cosmic ray muons in the test cell was calculated as a weighted average:

$$\Delta_{mp}^{cosmic} = \int_{E_{min}}^{\infty} E^{-2} \Delta_{mp}(E) dE / \int_{E_{min}}^{\infty} E^{-2} dE, \quad (6.4)$$

where  $E_{min}$  is taken as the minimum trigger energy 235 MeV of our telescope, and the upper limit of the integrals was truncated at 25 GeV. The value of calculated  $\Delta_{mp}^{cosmic}$  was largely insensitive to the exact value of the upper limit. The assumption that the test cell was exposed to only those cosmic rays in the  $E^{-2}$  part of spectrum is based on the fact that the experiment was carried out in a basement laboratory, with approximately three meters of concrete lying above, i.e., incident cosmic rays in the low energy part of the spectrum were stopped in the building material above the experiment.

A numerical calculation of (6.4) gives the result  $\Delta_{m.p.}^{cosmic} = 1.225 \text{ MeV}$ . This calculation is based on the assumption that all cosmic rays were incident on the test cell parallel to the electric field (perpendicular to the electrodes). As discussed in section 4.2.4 however, the actual mean path length of cosmic rays in the test cell is slightly larger than the electrode separation, so the most probable energy loss must be increased by a factor of 1.0044 (equation 4.11):

$$\Delta_{mp}^{cosmic} = 1.225 \text{ MeV} \times 1.0044 = 1.231 \pm 0.01 \text{ MeV}. \quad (6.5)$$

The uncertainty of the calculated value of  $\Delta_{mp}^{cosmic}$  was estimated by varying various parameters used in the calculation, the only variations having any substantial effect being a 5% change in  $E_{min}$ , a 10% change in the ionization potential  $I$ , and a 10% change in the exponent of the energy dependence of the incident cosmic ray flux.

### 6.3 The Most Probable Number of Electrons

The first step in obtaining the most probable number of free electrons  $Q_0(E)_{mp}$  liberated at each field strength was to produce pulse height distributions, one for each field strength, of charge liberated in the test cell.

The pulse height distributions were produced by using a least squares fitting routine to fit each individual pulse for  $Q_0$  only, with  $t_0$ ,  $\tau_l$ , and  $\mu$  held fixed at their measured values.

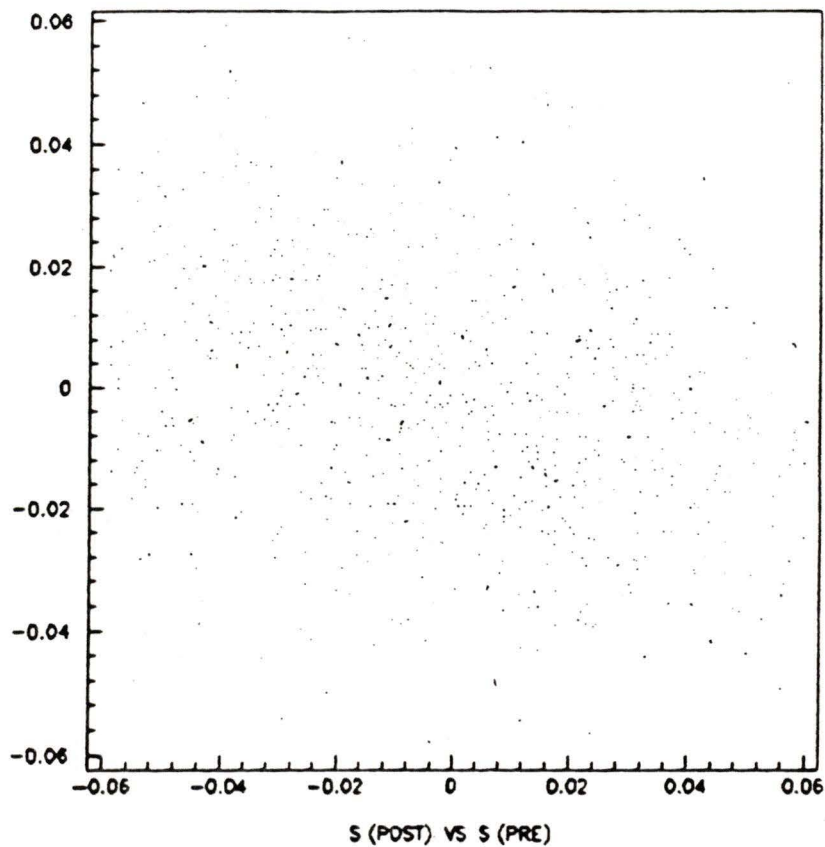


Figure 6.1:  $Slope_{pre}$  vs.  $Slope_{post}$

Since the background noise is a much more serious problem in single pulse fits than for averaged pulse fits, it was not immediately obvious how to handle the background levels in the single pulse fits. Two strategies were considered. The first strategy was to handle the background level the same way it was handled in the fits to the averaged pulses, i.e., fit a constant level (zero slope) to the pretrigger region and use that level as the baseline

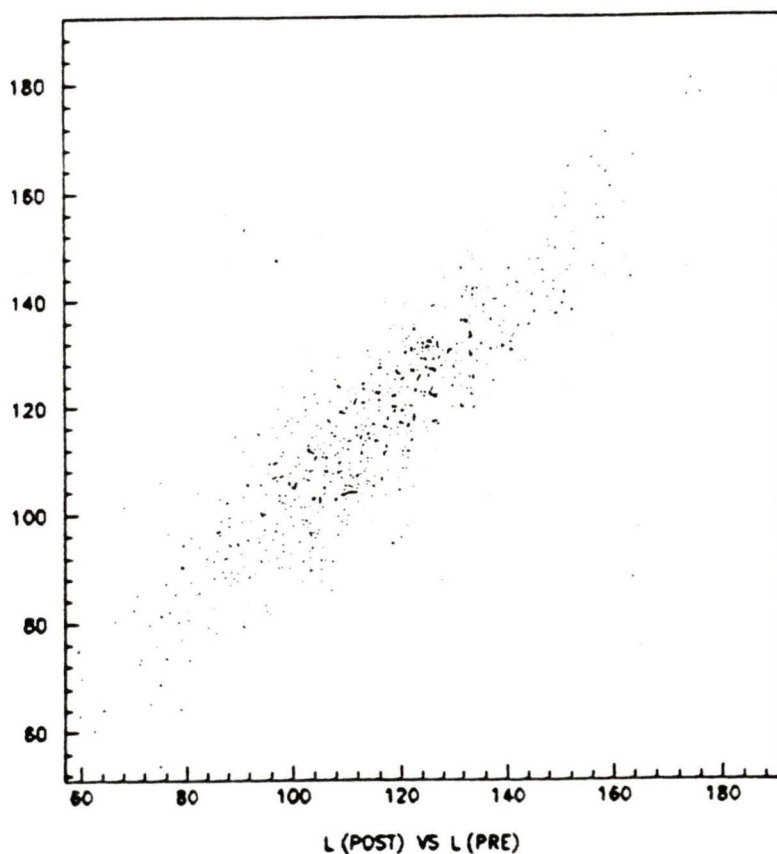


Figure 6.2:  $Level_{pre}$  vs.  $Level_{post}$

under the pulse. The second strategy considered was to fit a line (slope and intercept) to the pretrigger region, and extrapolate the fitted line through the region of the pulse as the baseline. The validity of each of these two strategies was tested by acquiring a set of random trigger data, i.e., the data acquisition was set to trigger on counts from a plastic scintillator placed well away from the test cell. The pulses thus obtained were therefore purely noise, not associated with cosmic rays passing through the test cell. The pretrigger region (first 1/4 of the pulse) and post-trigger region (last 3/4 of the pulse) of

each "random noise" pulse was then fitted with a constant level and also with a straight line. Scatter plots were then made of the fitted constant levels of the pre-trigger versus post-trigger regions (fig 6.2), and of the fitted slopes of the two regions (fig 6.1). It is apparent from fig 6.2 that the constant levels in the pre- and post-trigger regions are highly correlated, whereas from fig 6.1 it is apparent that there is little if any correlation in fitted slopes in the two regions. On the basis of this test, we opted for the first strategy, i.e., the background levels were taken as constant levels obtained from fits to the pretrigger regions.

Ten pulse height distributions were then produced by histogramming the fitted  $Q_0$ 's for each field strength. The most probable number of free electrons was obtained by finding the peak position of each histogram, accomplished by fitting a Gaussian line shape to the region of the peak in each histogram. An example of a pulse height distribution and fit are shown in fig 6.3. The centroid of the Gaussian was taken as the peak position, with care being taken not to use too large a fitting window that might bias the fit due to the asymmetry of the Landau distribution. Systematic fitting errors were estimated by repeating the peak fits with a third order Chebychev polynomial, the difference between this and the Gaussian fit results being taken as the error. These systematic errors were then added quadratically to the statistical errors of the Gaussian fits to estimate the total fitting errors.

The statistical uncertainties in the fitted  $Q_0$ 's were also taken into consideration. These uncertainties had the effect of broadening each of the pulse height distributions, analogous to instrumental resolution. Due to the asymmetry of the Landau distribution, any broadening of the distribution has the effect of increasing the apparent most probable point. This effect was estimated for each pulse height distribution by averaging the statistical uncertainties in the fitted  $Q_0$ 's, assuming these uncertainties are distributed

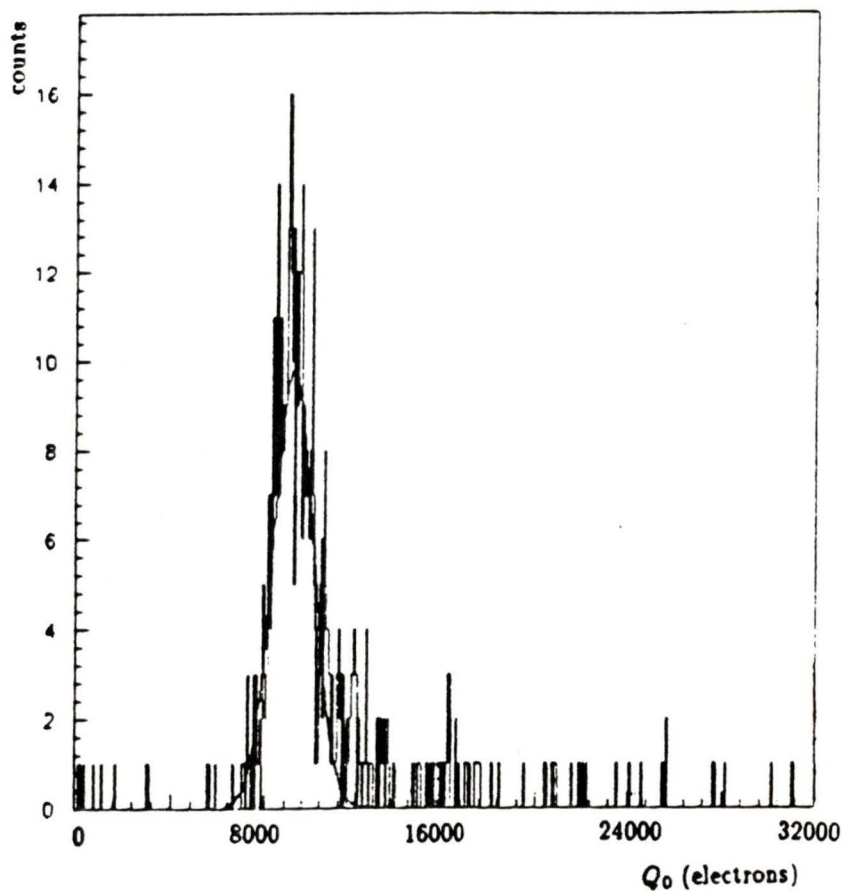


Figure 6.3: Pulse height histogram and fitted curve at 250V

as a Gaussian, then using Monte Carlo methods to estimate the effect on the determination of each  $Q_0(E)_{mp}$ . The typical effect was a downward shift of about 1%. The results of the determination of each  $Q_0(E)_{mp}$  are summarized in table 6.1. The column labeled "points" in the table is the number of data points in a fitting window. Fig 6.4 shows a sample pulse height spectrum with a Monte Carlo reconstruction superimposed.

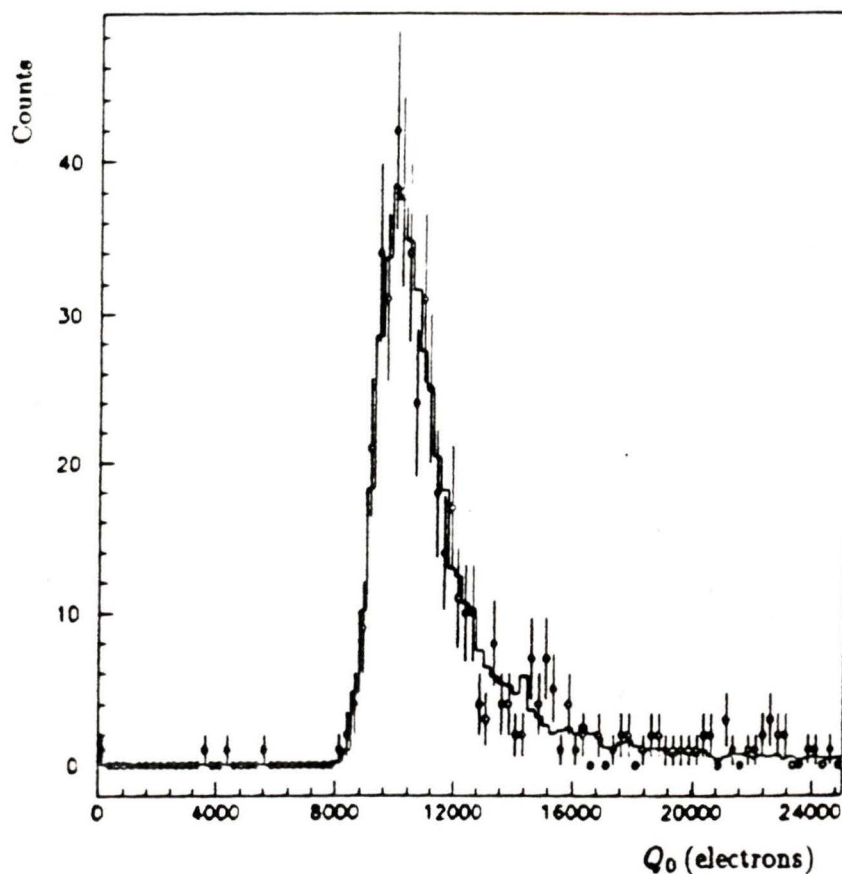


Figure 6.4: Pulse height data and Monte Carlo at 1500 V

#### 6.4 $G_{fi}(E)$ Curve and Fitted $G_{fi}(0)$

The 100 eV free ion yield  $G_{fi}(0)$  at zero field was obtained by fitting the data of table 6.1 to the Onsager formula (2.18). After inserting the numerical values for the dielectric constant  $\epsilon$  and temperature  $T$  ( $T=293 \pm 2$  K during data acquisition), and numerically calculating the definite integrals, the Onsager formula becomes

$$G_{fi}(E) = G_{fi}(0)(1 + 5.071 \times 10^{-5}E - 6.780^{-10}E^2 + \dots), \quad (6.6)$$

E (kV/cm)	$Q_0(E)_{mp}$ (electrons)	error	points	$\frac{Q_0(E)_{mp}}{\Delta_{mp}}$ (# e/100eV)
0.25	9109	103	199	0.7400
0.5	9336	118	200	0.7584
0.75	9352	470	195	0.7597
1.0	9530	64	163	0.7742
1.5	9903	101	205	0.8045
2.0	10260	69	197	0.8335
2.5	10471	131	253	0.8506
3.0	10665	199	214	0.8664
3.5	10989	201	219	0.8927
4.0	11005	173	233	0.8940

Table 6.1: The most probable charge at different field

where the electric field  $E$  is expressed in volts/cm.

The result of the fit is  $G_{fi}(0) = 0.743 \pm 0.002$  electrons/100eV, with a  $\chi^2/dof=1.2$ . The error quoted is statistical only. The data and fit are shown in fig 6.5.

A number of systematic uncertainties in the determination of  $G_{fi}(0)$  were also considered. Since the above pulse height distributions had been calculated using nominal values for  $\mu$  and  $\tau_l$ , the distributions were recalculated using values one  $\sigma$  from nominal. The ten resultant  $Q_0(E)_{mp}$ 's were then fitted as above. We repeated the  $G_{fi}(0)$  fits also with various other parameters set at one  $\sigma$  from nominal, including temperature (0.7%), plate gap (1%), dielectric constant (1%), calculated  $\Delta_{mp}$  (0.8%), and charge sensitivity (3.6%). Also considered was the effect of changing by 30% the downward shift in  $Q_0(E)_{mp}$  due to the "statistical uncertainty" broadening of the pulse height distribution. The largest effect by far of those considered was that due to the uncertainty in charge sensitivity. The effects of all these changes on the fitted  $G_{fi}(0)$  were then added in quadrature along with the statistical

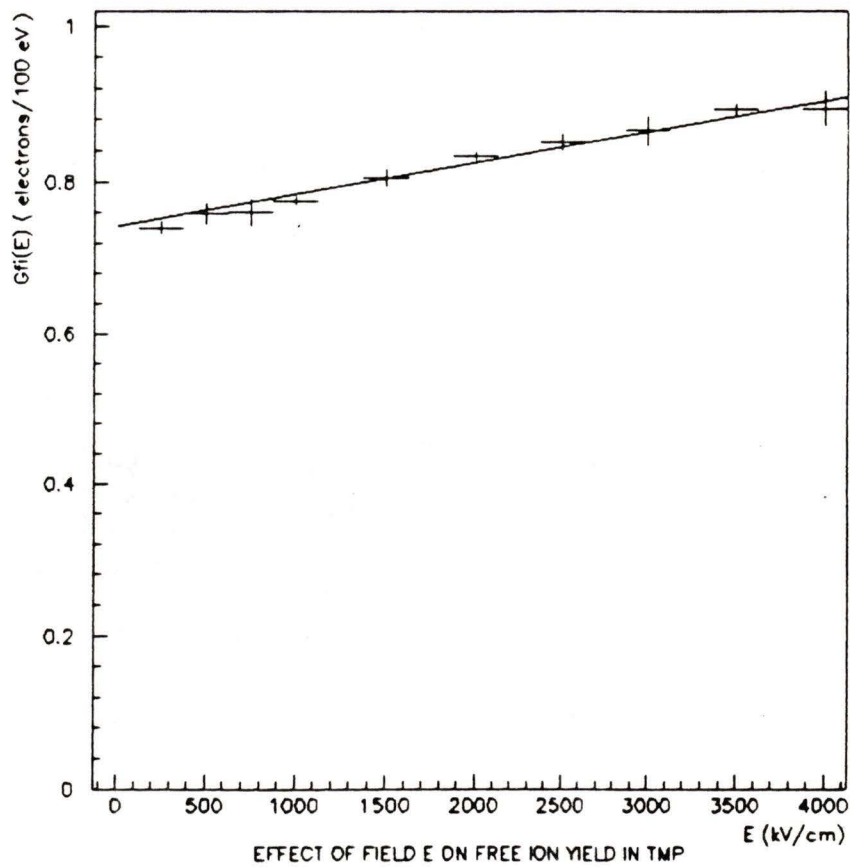


Figure 6.5: Free ion yield: data and fitted curve

error to give the result

$$G_{fi}(0) = 0.743 \pm 0.029 \text{ electrons}/100\text{eV}.$$

## Chapter 7

### Conclusion

The use of transient analysis in measuring the electron mobility, free ion yield, and achievable electron lifetime in TMP proved to be very successful. Not only were these properties measured, but realistic estimates of their uncertainties were also calculated. The electron lifetime of our TMP sample was measured to be

$$\tau_l = 121 \pm 19 \mu s$$

which demonstrates that our purification scheme worked well. It should be emphasized that this level of purity was achieved with physical purification techniques only (other groups [9] have used sodium/potassium alloy in their purification scheme), and that the TMP sample had previously been exposed to atmospheric air for several months without permanent adverse affects. Since the drift time for electrons in a real sampling calorimeter is typically only a few micro-seconds or less, this level of purity is more than sufficient.

The electron mobility in TMP was shown to be constant over the electric field strengths used in this work. Also, the field dependence of the free ion yield was shown to be correctly predicted by Onsager theory. The measured values of electron mobility and zero field free ion yield from this work are compared with previous measurements in table 7.1. The agreement

year	$\mu$ ( $cm^2V^{-1}s^{-1}$ ) (method)	$G_{fi}(0)(e/100eV)(method)$	ref.
1972	24 (pulse conductivity)	0.83 (charge collection)	[8]
1978	29 (pulse conductivity)	0.71 (charge clearing)	[14]
1988	$28 \pm 2$ (transient $t_d$ measurement)		[18]
1989	28 (transient $t_d$ measurement)		[16]
1990	$26.3 \pm 0.8$ (WFA)	$0.743 \pm 0.029$ (WFA)	

Table 7.1: Comparison of  $\mu$  and  $G_{fi}(0)$  measurements in room temperature 2,2,4,4 TMP

liquid	$\mu$ ( $cm^2V^{-1}s^{-1}$ )	$G_{fi}(0)$ (electrons/100eV)	reference
2,2,4,4 TMP	26.3	0.743	
TMS	95	0.74	[9]
2,2,3,3 TMP	5.2	0.42	[13]
2,2,4 TMP	5.3	< 0.39	[13]
2,2,5,5 TMH	12	0.67	[13]

Table 7.2: Comparison of  $\mu$  and  $G_{fi}(0)$  of 2,2,4,4 TMP with other candidates

is quite good, even though the methods of measurement differed radically.

Finally, the mobility and zero field free ion yield of TMP are compared with several other calorimeter candidate liquids in table 7.2. One can see from the table that only TMS, with its higher mobility, is competitive with 2,2,4,4 TMP. TMS however boils at  $26.5^\circ C$  and is also much more flammable than 2,2,4,4 TMP, which certainly reduces its attractiveness.

## Bibliography

- [1] J. J. Thomson, *Nature* 55 (1897) 606.
- [2] P. H. Tewari and J. R. Freeman, *J. Chem. Phys.* 49 (1968) 2197.
- [3] W. F. Schmidt and A. O. Allen, *J. Chem. Phys.* 50 (1969) 5037.
- [4] W. F. Schmidt, *Can. J. Chem.* 55 (1977) 2197.
- [5] R. Wigmans, *Nucl. Instr. and Meth.* A259 (1987) 389.
- [6] C. W. Fabjan, *Calorimetry in High-energy Physics*, CERN-EP/85-54 (1986).
- [7] J-P. Dodelet and G. R. Freeman, *Can. J. Chem.* 49 (1971) 2643.
- [8] J-P. Dodelet and G. R. Freeman, *Can. J. Chem.* 50 (1972) 2667.
- [9] A. Gonidec et al., *Ionization Chambers with Room Temperature Liquids for Calorimetry*, CERN-EP/88-36 (1988).
- [10] C. Bacci et al., *Analysis of the Signal Produced by Cosmic Rays in Liquid TMP*, UA1/TN 86-85 (1986).
- [11] R. Bonino and S. Veneziano, *A Waveform Analysis System for TMP Ionisation Chambers*, UA1/TN 88-13 (1986).

- [12] J. Engler and H. Keim, Nucl. Instr. and Meth. 223 (1983) 47.
- [13] A. O. Allen, Drift Mobilities and Conduction Band Energies of Excess Electrons in Dielectric Liquids, NSRDS-NBS 58 (1976).
- [14] T. G. Ryan and G. R. Freeman, J. Chem. Phys. 68 (1978) 5144.
- [15] R. A. Holroyd and D. F. Anderson, Nucl. Instr. and Meth. A236 (1985) 294.
- [16] K. Itoh et al., J. Chem. Phys. 90 (1989) 1128.
- [17] Handbook of Chemistry and Physics, CRC Press (1989) C-395.
- [18] A. Gonidec et al., On Measurements of Electron and Positive Ion Mobilities in Liquid TMP, UA1/TN 87-66 (1987).
- [19] R. C. Fernow, Introduction to Experimental Particle Physics, Cambridge University Press (1986) 40.
- [20] R. M. Sternheimer, Interaction of Radiation with Matter, Methods of Experimental Physics 5A, Academic Press (1961) 1.
- [21] J. E. Moyal, Phil. Mag. 6 (1955) 263.
- [22] P. V. Vavilov, Sov. Phys. JETP 5 (1978) 749.
- [23] L. Onsager, Phys. Rev. 54 (1938) 554.
- [24] S. P. Ahlen, Rev. Mod. Phys. 52 (1980) 143.
- [25] A. Mozumder, J. Chem. Phys. 48 (1972) 1659.
- [26] A. Mozumder, J. Chem. Phys. 50 (1969) 3153.

- [27] A. Mozumder, *J. Chem. Phys.* 50 (1969) 3162.
- [28] P. Ludwig, *J. Chem. Phys.* 50 (1969) 1787.
- [29] A. W. Wolfendale, Cosmic Rays, George Newnes Limited (1963) 128.
- [30] A. W. Wolfendale, Cosmic Rays at Ground level, The Institute of Physics (1973) 57.
- [31] G. N. Fowler and A. W. Wolfendale, *Handb. Phys.* 46/1 (1961) 274.
- [32] Particle Data Group, *Phys. Lett.* B204 (1988) 61.
- [33] F. James and M. Roos, MINUIT-Function Minimization and Error Analysis, CERN Program Library (1989).
- [34] R. M. Sternheimer et al., *Phys. Rev.* B26 (1982) 6067.
- [35] A. Astbury et al., (to be published in *Nucl. Instr. and Meth.*).
- [36] L. J. Geis, Transform Analysis and Filters, Prentice Hall (1989) 1.
- [37] R. A. Holroyd et al., *J. Phys. Chem.* 89 (1985) 2909.
- [38] R. C. Munoz et al., *J. Chem. Phys.* 85 (1986) 1104.

## VITA

Surname: Li Given Name: Yuhang

Place of Birth: Beijing, China Date of Birth: June 5, 1961

### Educational Institutions Attended:

University of Victoria	1987 to 1990
Institute of High Energy Physics, Academia Sinica	1983 to 1986
University of Science and Technology of China	1978 to 1983

### Degree Awarded:

M.Sc.	Institute of High Energy Physics, Academia Sinica	1986
B.Sc.	University of Science and Technology of China	1983

### Publications:

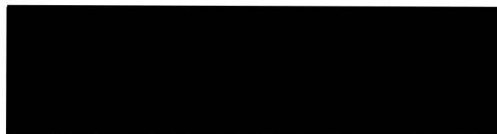
1. "Measurement of Properties of a Wire Chamber in Self Quench Streamer Mode", Symposium of Chinese Conference of Nuclear Physics, 1983
2. " $\gamma$ -ray Observation of the Crab Pulsar", High Energy Physics (Chinese Journal), Vol.2, 1985
3. "Determination of the Mixed Shape of High Altitude Balloon", Balloon Technology, COSPAR, 1986

PARTIAL COPYRIGHT LICENSE

I hereby grant the right to lend my thesis to users of the University of Victoria Library, and to make single copies only for such users or in response to a request from the Library of any other university, or similar institution, on its behalf or for one of its users. I further agree that permission for extensive copying of this thesis for scholarly purposes may be granted by me or a member of the University designated by me. It is understood that copying or publication of this thesis for financial gain shall not be allowed without my written permission.

Title: The Electronic Response of 2,2,4,4 Tetramethylpentane  
to Minimum Ionizing Particles

Author



Yuhang Li

November 6, 1990